可信推断近场稀疏综合阵列三维毫米波成像(中文/English)

杨 磊* 霍 鑫 申瑞阳 宋 昊 胡仲伟*

(中国民航大学电子信息与自动化学院 天津 300300)

摘要：考虑到主动式电扫描毫米波成像系统在实际应用中成像场景要求大，分辨率要求高，但毫米波的波长短，继而造成满足奈奎斯特采样定理的均匀阵列规模及馈电网络复杂度过高，面临着成像精度、成像速度和系统成本之间的矛盾。针对以上问题，该文提出了可信推断近场稀疏综合阵列算法(CBI-SAS)，在全贝叶斯学习框架下，该算法基于贝叶斯推断对复激励权值进行稀疏优化，得到复激励权值的完全统计后验概率密度函数，从而利用其高阶统计信息得到复激励权值的最优值及其置信区间和置信度。在贝叶斯推断中，为了实现较少数量的阵元合成期望波束方向图，可通过对复值激励权值引入重尾的拉普拉斯稀疏先验。然而，由于先验概率模型与参考方向图数据模型非共轭，因此需对先验模型进行分层贝叶斯建模，从而保证得到的复激励权值完全后验分布具有闭合解析解。为了避免求解完全后验分布的高维积分，采用变分贝叶斯期望最大化方法计算复激励权值后验概率密度函数，实现复激励权值的可信推断。仿真模拟实验结果显示，相较于传统稀疏阵列合成方法，所提方法阵元稀疏度更低、归一化均方误差更小、匹配方向图精度更好。此外，基于设计的稀疏阵列采集近场一维电扫和二维平面全电扫实测回波数据后，利用改进三维时域算法进行三维重建，验证了所提CBI-SAS算法在保证成像结果的同时降低了系统复杂性的优势。

关键词：毫米波成像；贝叶斯推断；稀疏阵列合成；分层贝叶斯；变分贝叶斯期望最大

中图分类号：TN957 **文献标识码**：A **文章编号**：2095-283X(2024)05-1092-17

DOI: 10.12000/JR24097

引用格式：杨磊, 霍鑫, 申瑞阳, 等. 可信推断近场稀疏综合阵列三维毫米波成像[J]. 雷达学报(中英文), 2024, 13(5): 1092–1108. doi: 10.12000/JR24097.

Reference format: YANG Lei, HUO Xin, SHEN Ruiyang, *et al*. Credible inference of near-field sparse array synthesis for three-dimensional millimeter-wave imagery[J]. *Journal of Radars*, 2024, 13(5): 1092–1108. doi: 10.12000/JR24097.

Credible Inference of Near-field Sparse Array Synthesis for Three-dimensional Millimeter-wave Imagery (in English)

YANG Lei* HUO Xin SHEN Ruiyang SONG Hao HU Zhongwei*

(*College of Electronic Information and Automation*, *Civil Aviation University of China*, *Tianjin* 300300, *China*)

Abstract: Due to the short wavelength of millimeter-wave, active electrical scanning millimeter-wave imaging system requires large imaging scenarios and high resolutions in practical applications. These requirements lead to a large uniform array size and high complexity of the feed network that satisfies the Nyquist sampling theorem. Accordingly, the system faces contradictions among imaging accuracy, imaging speed, and system cost. To this end, a novel, Credible Bayesian Inference of near-field Sparse Array Synthesis (CBI-SAS)

收稿日期：2024-05-22；改回日期：2024-08-05；网络出版：2024-08-26

*通信作者： 胡仲伟 zwhu@cauc.edu.cn； 杨磊 yanglei840626@163.com

*Corresponding Authors: HU Zhongwei, zwhu@cauc.edu.cn; YANG Lei, yanglei840626@163.com

基金项目：国家自然科学基金(62271487)，中央高校基本科研业务费(3122023PT04)

Foundation Items: The National Natural Science Foundation of China (62271487), Fundamental Research Funds for the Central Universities (3122023PT04)

责任主编：邓彬 Corresponding Editor: DENG Bin

algorithm is proposed under the framework of sparse Bayesian learning. The algorithm optimizes the complex-valued excitation weights based on Bayesian inference in a sparse manner. Therefore, it obtains the full statistical posterior Probability Density Function (PDF) of these weights. This enables the algorithm to utilize higher-order statistical information to obtain the optimal values, confidence intervals, and confidence levels of the excitation weights. In Bayesian inference, to achieve a small number of array elements to synthesize the desired beam orientation pattern, a heavy-tailed Laplace sparse prior is introduced to the excitation weights. However, considering that the prior probability model is not conjugated with the reference pattern data probability, the prior model is encoded in a hierarchical Bayesian manner so that the full posterior distribution can be represented in closed-form solutions. To avoid the high-dimensional integral in the full posterior distribution, a variational Bayesian expectation maximization method is employed to calculate the posterior PDF of the excitation weights, enabling reliable Bayesian inference. Simulation results show that compared with conventional sparse array synthesis algorithms, the proposed algorithm achieves lower element sparsity, a smaller normalized mean square error, and higher accuracy for matching the desired directional pattern. In addition, based on the measured raw data from near-field 1D electrical scanning and 2D plane electrical scanning, an improved 3D time domain algorithm is applied for 3D image reconstruction. Results verify that the proposed CBI-SAS algorithm can guarantee imaging results and reduce the complexity of the system.

Key words: Millimeter-wave imagery; Bayesian inference; Sparse array synthesis; Hierarchical Bayesian; Variational Bayesian expectation maximization

1　引言

近年来，国际上恐怖活动时有发生，对人类社会的发展与稳定造成挑战，故而对民航机场、汽车客运站、火车站等人流量较大场所的安检设备提出更高要求。传统的安检设备有手持式金属探测器、X射线安检机等，其中手持式金属探测器可以探测金属危险品，但对非金属类危险品无效，且探测范围有限，探测效率低下[1]。X射线安检机在探测效率、探测精度方面优于金属探测器，但是X射线的电离会对人体的健康造成辐射伤害，不宜对人体进行安检。随着毫米波器件及集成电路技术的快速发展，基于毫米波三维成像的安检技术已经成为研究热点。毫米波的频段位于30～300 GHz，波长位于1～10 mm范围，可以轻松穿透人体的表层衣物实现对隐匿危险品的探测，且无黑体效应，不会对人体造成辐射积累[2]。但是实际安检情况下需要覆盖大的成像范围，实现高的成像分辨率，然而毫米波的波长较短，对于满足二分之一波长的均匀阵列来说，系统需要大量的收发天线元件，阵元数目巨大，同时工作在高频段可能会出现阵元之间的相互耦合，导致实际系统设计复杂、工程实现困难、成本较高[3]。如今在毫米波阵列成像上大部分采用传统的三维重建算法，难以实现实时的高分辨成像，使得传统方式下的阵列成像在实际工程应用中面临着成像精度、成像速度和系统成本之间的矛盾，难以调和。

毫米波安检成像中，为了提高近场能量的聚焦效果，安检系统可以利用具有合适旁瓣电平、主瓣宽度以及指向性的波束方向图来捕获人体的三维信息。近年来，国内外学者提出了许多分析方法来解决天线阵列综合问题，包括均匀分布天线阵列的道尔夫-切比雪夫和泰勒方法[4,5]，这些方法降低了峰值旁瓣电平，但是增加了主瓣宽度。此外，这些均匀分布、等间距的阵列要想获得高分辨率的图像，需要大量的阵元，硬件成本高，计算复杂度大。为了解决这些问题，稀疏阵列综合技术应运而生，不但可以有效减少所需的阵元数目，同时可以确保合适的波束方向图。稀疏阵列综合技术的目标是基于一定的约束条件，如元素排列、权重范围等，进行优化天线阵列的空间响应性能，如主瓣宽度和旁瓣电平等，得到实现特定空间响应性能的最小阵元数目[6]。目前稀疏阵列综合主要集中在远场方面，文献[7]采用子采样分布来扩大单元间距，而这只能抑制伪贝塞尔波束的产生。文献[8]提出了一种基于子阵列的聚焦阵列天线，以减少天线的数量，但它具有较高的旁瓣电平(Side Lobe Level, SLL)。文献[9]采用遗传算法来合成可控的SLL稀疏阵列。然而，随机优化的方法耗时长，且存在局部收敛的问题。借鉴压缩感知(Compressed Sensing, CS)具有确定最优解的优势，在生物医学、稀疏阵列综合等各个研究领域都得到了广泛的应用。稀疏阵列综合中为了获得稀疏度最小的阵列，引入了先验和似然信息，在文献[10,11]中分别使用了单任务的贝叶斯压缩感知(Bayesian Compressed Sensing, BCS)和多任务的BCS，二者通过相关向量机(Relevance Vector Machine, RVM)进行求解，有效地解决了稀疏

阵列综合问题。由于阵列的激励由幅值和相位组成，是一个复数，然而单任务的BCS只能解决实数激励问题，而多任务的BCS适用于解决复激励问题，但是二者都是基于点估计来求解，激励权值的适应能力不强。因此，现有的稀疏阵列综合技术大都集中在远场均匀阵列的稀疏化过程，且面临着求解困难、局部收敛以及权值适应性不强的问题，对稀疏阵列成像处理方面却鲜有人研究。

通过所设计的稀疏阵列采集得到回波后进行高分辨成像，近场稀疏阵列成像常用的是时域成像算法和频域成像算法。典型的近场时域成像算法是后向投影算法(Back Projection Algorithm, BPA)，成像原理简单易实施[12]，可以适用于多种成像场景。但是，时域算法首先需要对成像场景划分网格，然后对每一个点相干积累成像，以此保证成像精度，运算量与阵元数目及成像场景中的像素点数成正比，应用于三维成像时运算效率较低。与时域算法相比，频域算法是将回波信号变换到空间域中进行补偿，避免了划分成像场景中的网格数，降低了运算量，提高了效率。典型的近场频域成像算法是距离徙动算法(Range Migration Algorithm, RMA)，其在成像的过程中需要利用插值在波数域进行补偿[13]，但是有限长的插值核函数会引入截断误差，降低成像精度。因此，在成像精度和成像速度上存在矛盾，难以满足如今的人体安检成像的需求。

基于以上分析，本文提出了可信推断近场稀疏综合阵列三维毫米波成像算法。将近场稀疏阵列综合建模为模式匹配问题，将合成的稀疏阵列方向图与期望目标方向图之间的误差等效转化为贝叶斯推断问题，使用贝叶斯压缩感知来确定接近目标参考方向图的稀疏度最小的阵列，该算法首先将复激励权值建模为拉普拉斯先验，由于先验与似然的非共轭特性，然后在先验建模的基础上，进行分层贝叶斯建模，构建似然函数与拉普拉斯先验参数之间的联系，进而推导出复激励权值的后验概率密度函数。此外，为了保证后验概率密度函数的闭合解析解，应用变分贝叶斯期望最大化(Variational Bayesian Expectation Maximization, VB-EM)方法，基于高斯-赛德尔迭代策略分别计算出复阵列权值及其超参数的后验概率密度函数。最后，利用后验概率密度函数的结果，得出复阵列权值的解析最优值以及置信区间和置信度，从而实现对复阵列权值动态变化的解析指示。在成像处理方面，通过所设计的稀疏阵列接收人体回波数据后进行分维处理，在高度-距离维运用快速分解后向投影算法(Fast Factorized Back Projection, FFBP)，首先将阵列分解为多个子孔径，然后通过线性插值递归融合相邻子图像，最后完成高度-距离维的二维重建，在方位-距离维运用后向投影算法完成方位-距离维的二维重建。本文在仿真实验中通过与传统的稀疏阵列合成方法对比，定量分析了本文所提方法在保持孔径不变的基础上，阵元稀疏度更小，合成方向图与目标方向图的匹配精度更好。在一维电扫和二维平面全电扫实测数据实验中，保持相同稀疏度情况下，本文所设计稀疏阵列在成像精度、成像速度和系统成本之间得到良好平衡。仿真对比模拟实验验证本文方法的有效性和优越性，一维电扫和二维平面全电扫实测数据验证了本文方法设计稀疏阵列重建的高精度。

2 电扫描成像系统及信号模型

毫米波电扫描成像系统采用在高度维线性阵列电扫描，方位维圆周扫描形成二维的合成孔径，以实现多角度的观察能力。这样既可以减少图像的重建次数，又可以提升系统扫描效率[14]，同时对三维回波数据进行采集，非常适合于近距离的安检成像。毫米波圆周扫描成像系统几何模型如图1所示，以原点O建立三维极坐标系(R,θ,Z)，被检测人员站在圆柱中心。天线阵列在Z方向形成间距为Δh的均匀线阵，线阵以Z轴为轴心，并且天线以R_0为半径绕着Z轴做轴心旋转，天线阵列在每个位置扫描完

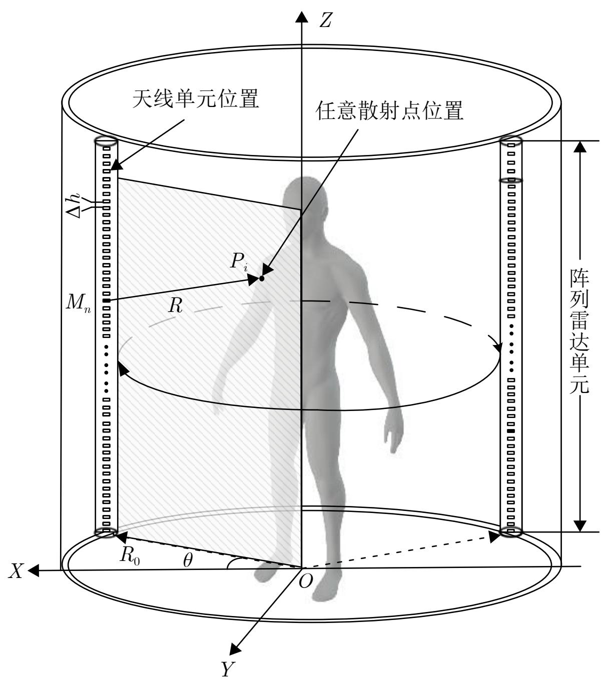

图 1 毫米波圆周扫描成像系统几何模型

Fig. 1 Geometric model of millimeter-wave electric scanning circumferential 3D imaging system

目标后，移动到下一个位置继续扫描直到结束，两个维度的扫描形成一个圆柱的扫描面。天线阵列的位置与X轴的夹角定义为θ，每次运动的角度间隔为$\Delta\theta$，天线的俯仰波束宽度与线阵旋转范围决定了高度-方位两维分辨率大小。

在毫米波一维电扫描圆周三维成像系统中，为保证成像分辨率，通常采用大时宽带宽信号，而常见的大时宽带宽信号为线性调频信号，其数学表达式为

$$s_{\mathrm{t}}(t)=\mathrm{rect}\left(\frac{t}{T_{\mathrm{p}}}\right)\exp\left\{\mathrm{j}2\pi\left(f_{\mathrm{c}}t+\frac{\gamma}{2}t^2\right)\right\} \tag{1}$$

其中，t表示快时间，$\mathrm{rect}(\cdot)$为矩形窗函数，T_{p}表示发射信号时间宽度，f_{c}表示信号中心频率，即载频，γ为线性调频信号的调频斜率。

天线单元M_n的位置为$(R_0\cos\theta,R_0\sin\theta,z)$，目标散射点$P_i$的位置为$(x_i,y_i,z_i)$，则从天线单元$M_n$到目标散射点$P_i$的距离为

$$\begin{aligned}&R(\theta;z)\\&=\sqrt{(R_0\cos\theta-x_i)^2+(R_0\sin\theta-y_i)^2+(z-z_i)^2}\end{aligned} \tag{2}$$

经过时延后天线单元M_n接收到目标散射点P_i的原始回波信号为

$$\begin{aligned}&s_{\mathrm{r}}(t,\theta,z)\\&\quad=\sigma_i\mathrm{rect}\left(\frac{t-\tau(\theta;z)}{T_{\mathrm{p}}}\right)\\&\qquad\cdot\exp\left\{\mathrm{j}2\pi\left[f_{\mathrm{c}}(t-\tau(\theta;z))+\frac{\gamma}{2}(t-\tau(\theta;z))^2\right]\right\}\end{aligned} \tag{3}$$

其中，σ_i为第i个目标散射点的后向散射系数，回波延迟可以表示为$\tau(\theta;z)=2R(\theta;z)/\mathrm{c}$。

对式(3)进行下变频接收，获得的回波信号为

$$\begin{aligned}s(t,\theta,z)=&\,\sigma_i\mathrm{rect}\left(\frac{t-\tau(\theta;z)}{T_{\mathrm{p}}}\right)\\&\cdot\exp\left\{-\mathrm{j}2\pi f_{\mathrm{c}}\tau(\theta;z)+\mathrm{j}\pi\gamma(t-\tau(\theta;z))^2\right\}\end{aligned} \tag{4}$$

对式(4)通过匹配滤波进行脉冲压缩，通常选取发射信号线性调频部分的时域翻转共轭信号作为脉冲压缩的匹配滤波器，即

$$h(t)=\exp\{-\mathrm{j}\pi\gamma(-t)^2\} \tag{5}$$

脉冲压缩的过程通常通过信号的频域相乘来实现，即

$$\begin{aligned}s_O(t,\theta,z)&=\mathrm{FFT}^{-1}\{\mathrm{FFT}[s(t,\theta,z)]\cdot\mathrm{FFT}[h(t)]\}\\&=\sigma_i\,\mathrm{sinc}\left(\frac{t-\tau(\theta;z)}{T_{\mathrm{p}}}\right)\exp(-\mathrm{j}2\pi f_{\mathrm{c}}\tau(\theta;z))\end{aligned} \tag{6}$$

其中，FFT^{-1}表示快速傅里叶逆变换。由式(6)可见，回波信号经过匹配滤波的脉冲压缩处理后，在距离时域表现为sinc函数形式，说明回波已经完成距离维的聚焦，而在方位和高度维上仍需要聚焦处理。

3　稀疏阵列综合

贝叶斯压缩感知是用于合成阵列稀疏度最小的期望辐射方向图现有技术之一，具有灵活性和计算效率高等显著优势[15]，但是利用贝叶斯学习对近场稀疏阵列综合还鲜有人研究。在稀疏贝叶斯学习框架下，本文将近场稀疏阵列综合问题建模为模式匹配问题。由于该模式匹配问题是一个多项式复杂程度的非确定性(Non-deterministic Polynomial, NP)问题，难以用确定性方法求解，因此进一步将稀疏阵列综合问题表述为贝叶斯压缩感知模型。在贝叶斯学习中，考虑到现实中阵列规模大，阵元个数多的问题，而本文旨在使用尽可能少的阵元合成期望方向图，因此对复激励权值施加重尾的拉普拉斯稀疏先验，并对先验进行分层建模，最后通过贝叶斯推断求解给出最优稀疏阵列的激励的完全后验概率密度函数，进而得到其置信区间和置信度。

3.1　阵列复激励分层贝叶斯建模

本文考虑一个具有N个均匀各向同性阵元的圆周柱面线性阵列等效模型。在对近场阵列进行稀疏综合前，因为近场阵列接收端接收到的信号是目标向其辐射的球面波，因此首先需要对均匀阵列的近场聚焦阵列进行建模[16]，以该模型为依据进行稀疏阵列综合。本文对于不同高度处的目标聚焦，采用的是相同的阵列天线，阵列天线始终分布在高度维Z轴上，阵列孔径长度为1.8 m，当阵列天线旋转到某一个方位位置时，三维坐标系转化为二维坐标系，建立如图2所示的任意方位下近场阵列聚焦模型，将阵列天线的物理中心处的阵元作为参考阵元，记$O(0,0)$为笛卡儿坐标系的参考原点(假设阵元的总数为奇数)。

本文采用笛卡儿坐标系对近场阵列模型建模，因此只能对平行于阵列的直线进行截取，将其称为聚焦线，文献[17]中叙述到当聚集线略微大于阵列时，阵列在该范围内性能较好，效率较高。对于毫米波安检应用场景，人体中心距离高度维Z轴为0.628 m，因此设置聚焦线距离高度维Z轴为0.628 m，如图2所示的聚焦线3，为了最大限度地减小天线之间的互相干扰和耦合，选取聚焦线3上中心处的散射点P作为增益最大的点，即天线阵列的正交方向上进行近场阵列建模，以此提高天线阵列的聚焦性能。对于空间中的任意一个散射点$K(x_k,z_k)$，参考

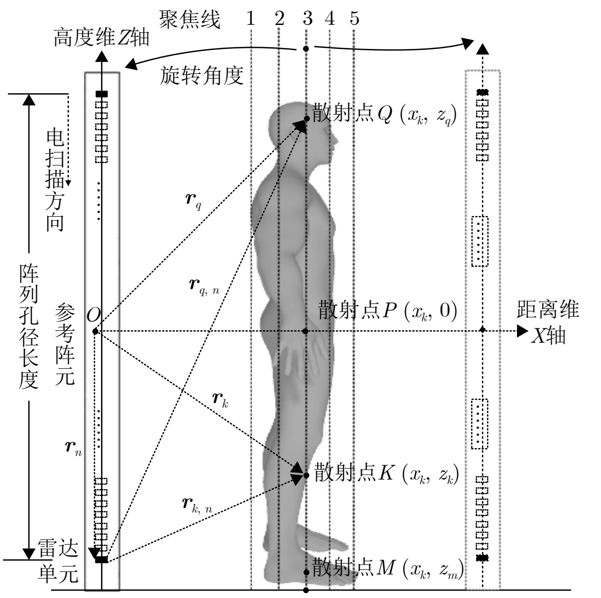

图 2 任意方位下近场线阵聚焦模型

Fig. 2 Focusing model of near-field linear array in Cartesian coordinate system with arbitrary orientation

点O指向散射点K的向量为$\boldsymbol{r}_k$，参考点O指向序号为n阵元的向量为$\boldsymbol{r}_n$，阵列中序号为n的阵元指向散射点K的向量为$\boldsymbol{r}_{k,n}=\boldsymbol{r}_k-\boldsymbol{r}_n$，则序号为$n$的阵元在散射点$K$辐射的电场为

$$\begin{aligned} E_n(\boldsymbol{r}_k) &= f_0(\theta,\psi)w_n\frac{\mathrm{e}^{-\mathrm{j}2\pi|\boldsymbol{r}_{k,n}|/\lambda}}{|\boldsymbol{r}_{k,n}|} \\ &= f_0(\theta,\psi)w_n\frac{\mathrm{e}^{-\mathrm{j}2\pi|\boldsymbol{r}_k-\boldsymbol{r}_n|/\lambda}}{|\boldsymbol{r}_k-\boldsymbol{r}_n|} \end{aligned} \tag{7}$$

其中，λ为阵列天线的工作波长，$f_0(\theta,\psi)$表示阵列中阵元方向图的单元因子，本文假定每个阵元都是理想全向性天线，即单元因子$f_0(\theta,\psi)=1$，w_n为序号n的阵元对应的复激励权值。通过假设线性阵列中阵元都是各向同性的，可以忽略阵元之间的相互耦合造成的干扰，显著简化阵列综合的分析和计算，突出介绍可信推断稀疏阵列综合算法的基本原理，对稀疏阵列进行初步的设计。实际系统中的阵元通常具有一定的方向性，在不同的方向性上具有不同的响应，全向阵元假设无法捕捉到这种方向性带来的偏差对成像的影响，下一步将会考虑由阵列方向性带来的相位误差进行校准[18]。因此，N个阵元的阵列天线在散射点K叠加所辐射的电场可以表示为

$$E(\boldsymbol{r}_k)=\sum_{n=1}^{N}w_n\frac{\mathrm{e}^{-\mathrm{j}2\pi|\boldsymbol{r}_k-\boldsymbol{r}_n|/\lambda}}{|\boldsymbol{r}_k-\boldsymbol{r}_n|} \tag{8}$$

在近场毫米波安检下，被测人体是三维立体，因此将$E(\boldsymbol{r}_k)$中的$\boldsymbol{r}_k$替换为近场观测区域内的距离向量来完成观测区域内的波束方向图的形成，基于叠加原理，线性阵列在近场区的观测点$E(\boldsymbol{r})$处辐射的电场表示为

$$E(\boldsymbol{r})=\sum_{n=1}^{N}w_n\frac{\mathrm{e}^{-\mathrm{j}2\pi|\boldsymbol{r}-\boldsymbol{r}_n|/\lambda}}{|\boldsymbol{r}-\boldsymbol{r}_n|} \tag{9}$$

其中，$\boldsymbol{r}$为近场观测点到参考点的距离向量。通过离散化，式(9)重写为如下的矩阵形式：

$$\boldsymbol{E}=\boldsymbol{\varPhi}\boldsymbol{w} \tag{10}$$

其中，$\boldsymbol{E}=[E(\boldsymbol{r}_{O1}),E(\boldsymbol{r}_{O2}),\cdots,E(\boldsymbol{r}_{OK})]^{\mathrm{T}}$为在不同的$K$个观测位置的样本向量，$\boldsymbol{w}=[w_1,w_2,\cdots,w_N]^{\mathrm{T}}$是$N$个阵元的复激励权值向量，$\boldsymbol{w}$中每一个元素的位置代表着天线阵元的位置，每一个元素的大小代表着天线阵元激励的幅度，近场毫米波安检下，导向向量矩阵$\boldsymbol{\varPhi}$可以写为

$$\boldsymbol{\varPhi}=\left\{\begin{matrix} \dfrac{\exp(-\mathrm{j}2\pi\,|\boldsymbol{r}_{O1}-\boldsymbol{r}_1|\,/\lambda)}{|\boldsymbol{r}_{O1}-\boldsymbol{r}_1|} & \dfrac{\exp(-\mathrm{j}2\pi\,|\boldsymbol{r}_{O1}-\boldsymbol{r}_2|\,/\lambda)}{|\boldsymbol{r}_{O1}-\boldsymbol{r}_2|} & \cdots & \dfrac{\exp(-\mathrm{j}2\pi\,|\boldsymbol{r}_{O1}-\boldsymbol{r}_N|\,/\lambda)}{|\boldsymbol{r}_{O1}-\boldsymbol{r}_N|} \\ \vdots & \ddots & \vdots \\ \dfrac{\exp(-\mathrm{j}2\pi\,|\boldsymbol{r}_{OK}-\boldsymbol{r}_1|\,/\lambda)}{|\boldsymbol{r}_{OK}-\boldsymbol{r}_1|} & \dfrac{\exp(-\mathrm{j}2\pi\,|\boldsymbol{r}_{OK}-\boldsymbol{r}_2|\,/\lambda)}{|\boldsymbol{r}_{OK}-\boldsymbol{r}_2|} & \cdots & \dfrac{\exp(-\mathrm{j}2\pi\,|\boldsymbol{r}_{OK}-\boldsymbol{r}_N|\,/\lambda)}{|\boldsymbol{r}_{OK}-\boldsymbol{r}_N|} \end{matrix}\right\} \tag{11}$$

稀疏阵列合成的目的是找到具有最少阵元数的阵列和相关联阵元的复激励权值，使其辐射方向图与期望的参考方向图$\boldsymbol{E}_{\mathrm{ref}}$匹配，匹配误差为$\boldsymbol{e}$，然后该问题可以转化为一个$\ell_0$范数约束的模式匹配优化问题，匹配模型如式(12)所示。

$$\min\ \|\boldsymbol{w}\|_0\ \text{s.t.}\ \|\boldsymbol{E}_{\mathrm{ref}}-\boldsymbol{\varPhi}\boldsymbol{w}\|_2^2<\boldsymbol{e} \tag{12}$$

其中，$\|\cdot\|_0$表示ℓ_0范数，约束了复激励权值$\boldsymbol{w}$非零的个数，而复激励权值$\boldsymbol{w}$的个数就是阵列中阵元的个数，因此约束了复激励权值$\boldsymbol{w}$非零的个数等价于约束了阵列中阵元非零的个数，$\|\cdot\|_2$表示ℓ_2范数，约束了稀疏阵列合成的方向图与参考方向图的匹配精度，$\boldsymbol{E}_{\mathrm{ref}}=[E_{\mathrm{ref}}(\boldsymbol{r}_{O1}),E_{\mathrm{ref}}(\boldsymbol{r}_{O2}),\cdots,E_{\mathrm{ref}}(\boldsymbol{r}_{OK})]^{\mathrm{H}}\in C^K$是近场参考方向图在不同的$K$个观测位置的样本向量，$\boldsymbol{e}=[e(\boldsymbol{r}_{O1}),e(\boldsymbol{r}_{O2}),\cdots,e(\boldsymbol{r}_{OK})]^{\mathrm{H}}\in C^K$是精度为$\boldsymbol{\beta}$的零均值复高斯误差向量。

式(12)表示的问题是一个NP难问题，难以用确定性的方法解决。随机优化可能是解决这一问题的候选方法，但是它面临着局部收敛的问题[19]，并且由于复杂高维问题而效果不佳。BCS已经被用来

在远场的稀疏阵列合成中[10]，为了将近场稀疏阵列合成问题表述为BCS问题，将式(12)中的ℓ_2范数约束进一步表示为

$$\boldsymbol{E}_{\text{ref}}= \boldsymbol{\varPhi}\boldsymbol{w} + \boldsymbol{e} \tag{13}$$

为了找到具有最少阵元数的阵列和阵元的复激励权值，使得辐射方向图与期望的参考方向图匹配，将难以用确定性方法求解的式(12)转化为式(13)贝叶斯压缩感知问题，本质上是将式(12)模式匹配问题中求解复激励权值$\boldsymbol{w}$的ℓ_0范数最小化问题转变为求解式(13)的复激励权值$\boldsymbol{w}$的完全后验分布的问题。

假设误差$\boldsymbol{e}$服从精度为$\boldsymbol{\beta}$的零均值对称复高斯分布，因此可得参考方向图$\boldsymbol{E}_{\text{ref}}$似然函数为

$$\begin{aligned} p(\boldsymbol{E}_{\text{ref}}\,|\boldsymbol{w},\boldsymbol{\beta}) &= \text{CN}(\boldsymbol{E}_{\text{ref}}\,|\boldsymbol{\varPhi}\boldsymbol{w},\,\boldsymbol{\beta}^{-1}\boldsymbol{I}) \\ &= \left(\frac{\boldsymbol{\beta}}{\pi}\right)^K \exp\left(-\boldsymbol{\beta}\,\|\boldsymbol{E}_{\text{ref}}-\boldsymbol{\varPhi}\boldsymbol{w}\|_2^2\right) \end{aligned} \tag{14}$$

考虑到误差的随机性，故对误差精度$\boldsymbol{\beta}$建模为伽马分布，建模如下：

$$p(\boldsymbol{\beta}\,|c,d) = \text{Gamma}(\boldsymbol{\beta}\,|c,d) = \frac{d^c}{\Gamma(c)}\boldsymbol{\beta}^{c-1}\exp(-d\boldsymbol{\beta}) \tag{15}$$

其中，$\Gamma(c)=\displaystyle\int_0^\infty t^{c-1}\mathrm{e}^{-t}\mathrm{d}t$为伽马函数，$c$, d为常参数[20]，根据经验值可取10^{-3}。

考虑到现实情况中阵列规模过大，成本过高，本文为了使用较少的阵元合成期望辐射的方向图，因此对复激励权值$\boldsymbol{w}$施以重尾的拉普拉斯稀疏先验[21,22]，当获得复激励权值的先验模型和似然函数后，可联合二者基于贝叶斯原理获得复激励权值的联合后验分布，再基于贝叶斯推断求解复激励权值后验解析解。然而，由于重尾的拉普拉斯稀疏先验与高斯似然函数非共轭，因此无法推导获得后验概率密度函数的闭合解析解。为此，本文通过引入中间超参数对重尾的拉普拉斯稀疏先验模型进行分层贝叶斯建模，以实现复数激励权值的完全后验概率密度函数的求解。

本文在分层模型的第1步将$\boldsymbol{w}$建模成为依赖于超参数$\boldsymbol{\alpha}$的复高斯分布，建模如下：

$$p(\boldsymbol{w}\,|\boldsymbol{\alpha}) = \prod_{i=1}^N \text{CN}(w_i\,|0,\alpha_i) = \prod_{i=1}^N \frac{1}{\pi\alpha_i}\exp\left(-\frac{w_i^2}{\alpha_i}\right) \tag{16}$$

由于高斯函数具有固有的平滑特性，式(16)不属于稀疏分布范围内。为促进先验的稀疏性与后验分布推导的简便，本文选取与高斯分布成对共轭的伽马分布作为超参数$\boldsymbol{\alpha}$的先验，并且在分层模型的第2步将超参数$\boldsymbol{\alpha}$建模如下：

$$\begin{aligned} p(\boldsymbol{\alpha}\,|a,b) &= \prod_{i=1}^N \text{Gamma}(\alpha_i\,|a,b) \\ &= \prod_{i=1}^N \frac{b^a}{\Gamma(a)}\alpha_i^{a-1}\exp(-b\alpha_i) \end{aligned} \tag{17}$$

根据式(16)和式(17)可以计算出复激励权值$\boldsymbol{w}$的边缘分布，即$p(\boldsymbol{w})=\displaystyle\int p(\boldsymbol{w}\,|\boldsymbol{\alpha})p(\boldsymbol{\alpha}\,|a,b)\mathrm{d}\boldsymbol{\alpha}$，当$a$的值为1.5时，该边缘分布服从拉普拉斯分布[20]，b根据经验值可取10^{-6}。上述分层贝叶斯模型中参数与超参数的概率模型如图3所示。图3中$\boldsymbol{E}_{\text{ref}}$为参考方向图，$\boldsymbol{w}$为待求的复激励权值，$\boldsymbol{\alpha}$和$\boldsymbol{\beta}$为引入的超参数随机变量，$\boldsymbol{w}$和$\boldsymbol{\alpha}$的分层能够将非共轭的问题实现可解性，从而简化模型，虚线方框中的a, b, c, d均为固定的参数。

3.2 阵列复激励变分推断求解

根据3.1节所给定的贝叶斯分层模型，应用贝叶斯推断理论计算激励权值$\boldsymbol{w}$和超参数$\boldsymbol{\alpha}$, $\boldsymbol{\beta}$的联合后验概率分布为

$$p(\boldsymbol{w},\boldsymbol{\alpha},\boldsymbol{\beta}\,|\boldsymbol{E}_{\text{ref}}) = \frac{p(\boldsymbol{E}_{\text{ref}}\,|\boldsymbol{w},\boldsymbol{\beta})p(\boldsymbol{w}\,|\boldsymbol{\alpha})p(\boldsymbol{\alpha})p(\boldsymbol{\beta})}{p(\boldsymbol{E}_{\text{ref}})} \tag{18}$$

式(18)中分子由式(14)—式(17)可以获得，然而，为了优化阵列中阵元的个数，需要计算复激励权值$\boldsymbol{w}$的完全后验分布，但计算式(18)中的分母项，它需要多维积分，这是很难处理的。为了合理的精度和效率，变分贝叶斯期望最大化(VB-EM)作为一种典型的确定性的近似算法，可以有效地进行隐随机变量的推断，并通过期望最大化方法获得随机变量的后验分布解析解。

本文将$\boldsymbol{w}$, $\boldsymbol{\alpha}$, $\boldsymbol{\beta}$, $\boldsymbol{E}_{\text{ref}}$视为随机变量，其中，$\boldsymbol{E}_{\text{ref}}$是可以测量的，是显随机变量，$\boldsymbol{w}$, $\boldsymbol{\alpha}$, $\boldsymbol{\beta}$是无法直接测量的，是隐随机变量，隐随机变量包含在$\boldsymbol{Z}=\{\boldsymbol{w},\ \boldsymbol{\alpha},\ \boldsymbol{\beta}\}$这个待求解的随机变量组合中，这些隐随机变量的后验概率密度函数可以通过VB-EM求解得到。则式(14)的对数似然函数可以表示为

$$\ln p(\boldsymbol{E}_{\text{ref}}) = \text{ELBO}(q) + \text{KL}(q\,\|p) \tag{19}$$

其中，

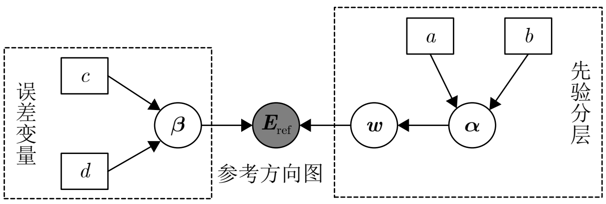

图 3 贝叶斯分层概率模型

Fig. 3 Bayesian graphic model

$$\mathrm{ELBO}(q)=\int q(\boldsymbol{Z})\ln\left(\frac{p(\boldsymbol{E}_{\mathrm{ref}},\boldsymbol{Z})}{q(\boldsymbol{Z})}\right)\mathrm{d}\boldsymbol{Z} \tag{20}$$

$$\mathrm{KL}(q\,\|p)=-\int q(\boldsymbol{Z})\ln\left(\frac{p(\boldsymbol{Z}\,|\boldsymbol{E}_{\mathrm{ref}})}{q(\boldsymbol{Z})}\right)\mathrm{d}\boldsymbol{Z} \tag{21}$$

其中，$q(\boldsymbol{Z})$是近似的后验概率密度函数，$\mathrm{ELBO}(q)$表示最低证据下界，$\mathrm{KL}(q\,\|p)$表示后验概率密度函数$p(\boldsymbol{Z}\,|\boldsymbol{E}_{\mathrm{ref}})$和近似后验概率密度函数$q(\boldsymbol{Z})$之间的散度(KL)。因为$\mathrm{KL}(q\,\|p)\ge 0$，所以$\ln p(\boldsymbol{E}_{\mathrm{ref}})\ge \mathrm{ELBO}(q)$，因此对数似然函数的增加始终大于下界的增加，从而最低证据下界保证了算法的收敛性。

在VB-EM算法中，根据平均场理论假设，我们可以通过将$q(\boldsymbol{Z})$进行因式分解来简化推导。由此，$q(\boldsymbol{Z})$可近似表示为

$$q(\boldsymbol{Z})\approx q(\boldsymbol{w})q(\boldsymbol{\alpha})q(\boldsymbol{\beta}) \tag{22}$$

基于式(22)的因式分解，VB-EM算法即是让下界$\mathrm{ELBO}(q)$相对于q最大化，将式(22)代入式(20)中，可以得到相应随机变量的解为

$$\hat{q}(\boldsymbol{Z}_i)\approx\exp\{<\ln p(\boldsymbol{E}_{\mathrm{ref}},\boldsymbol{Z})>_{q(\boldsymbol{Z})/q(\boldsymbol{Z}_i)}\}+\mathrm{const} \tag{23}$$

其中，$i=1, 2, 3$时对应$\boldsymbol{w}$, $\boldsymbol{\alpha}$, $\boldsymbol{\beta}$的后验概率密度函数序号，$<\cdot>_{q(\boldsymbol{Z})/q(\boldsymbol{Z}_i)}$表示关于$\boldsymbol{Z}$中除了$\boldsymbol{Z}_i$之外的期望算子。根据式(23)，$\boldsymbol{Z}$中的每一个元素的近似后验概率密度函数都可以被推断出来。

复激励权值$\boldsymbol{w}$的近似后验概率密度函数为

$$\hat{q}(\boldsymbol{w})\approx\exp\{<\ln p(\boldsymbol{E}_{\mathrm{ref}}\,|\boldsymbol{w},\boldsymbol{\beta})p(\boldsymbol{w}\,|\boldsymbol{\alpha})>_{q(\boldsymbol{\alpha})q(\boldsymbol{\beta})}+\mathrm{const}\} \tag{24}$$

将式(14)和式(16)代入式(24)中，可得到复激励权值$\boldsymbol{w}$服从复高斯分布

$$\hat{q}(\boldsymbol{w})\approx\prod_{m=1}^{N}\mathrm{CN}\left(w_m\,|\boldsymbol{\mu},\boldsymbol{\Sigma}\right) \tag{25}$$

其中，

$$\boldsymbol{\mu}=<\boldsymbol{\beta}>\boldsymbol{\Sigma}\boldsymbol{\Phi}^{\mathrm{H}}\boldsymbol{E}_{\mathrm{ref}} \tag{26}$$

$$\boldsymbol{\Sigma}=\left(<\boldsymbol{\beta}>\boldsymbol{\Phi}^{\mathrm{H}}\boldsymbol{\Phi}+<\boldsymbol{A}>\right)^{-1} \tag{27}$$

其中，$(\cdot)^{-1}$是求逆算子，上标H是共轭转置算子，$\boldsymbol{A}=\mathrm{diag}(\alpha_1^{-1}, \alpha_2^{-1}, \cdots, \alpha_N^{-1})$，式(26)的均值可以理解为稀疏复激励权值$\boldsymbol{w}$的最优值，当复激励权值$\boldsymbol{w}$的值小于最大值的0.03倍时，复激励权值设为零，此时该位置处没有阵元，式(27)为协方差矩阵，根据设置的显著性水平可以求出最优值的置信上限和下限，从而确定最优值的置信区间和置信度。

同理，根据式(23)可得超参数$\boldsymbol{\alpha}$的近似后验概率密度函数为

$$\hat{q}(\boldsymbol{\alpha})\approx\exp\{<\ln p(\boldsymbol{w}\,|\boldsymbol{\alpha})p(\boldsymbol{\alpha})>_{q(\boldsymbol{w})}+\mathrm{const}\} \tag{28}$$

将式(16)和式(17)代入式(28)中，可得到$\boldsymbol{\alpha}$的每个元素服从广义逆高斯分布，其第l阶距为

$$<\alpha_i^l>=\left(\frac{<2|w_i|^2>}{2b}\right)^{\frac{l}{2}}\frac{\mathcal{K}_{\eta-1+l}\left(\sqrt{2b<2|w_i|^2>}\right)}{\mathcal{K}_{\eta-1}\left(\sqrt{2b<2|w_i|^2>}\right)} \tag{29}$$

其中，$\mathcal{K}_a$为第2类修正贝塞尔函数[20]，当令$l=-1$时，更新后的$<\alpha_i^{-1}>$用于式(27)。

同理，根据式(23)可得超参数$\boldsymbol{\beta}$的近似后验概率密度函数为

$$\hat{q}(\boldsymbol{\beta})\approx\exp\{<\ln p(\boldsymbol{E}_{\mathrm{ref}}\,|\boldsymbol{w},\boldsymbol{\beta})p(\boldsymbol{\beta})>_{q(\boldsymbol{w})q(\boldsymbol{\beta})}+\mathrm{const}\} \tag{30}$$

将式(14)和式(15)代入式(30)中，可得到$\boldsymbol{\beta}$服从伽马分布，$\boldsymbol{\beta}$的均值为

$$<\boldsymbol{\beta}>=\frac{K+c}{\|\boldsymbol{E}_{\mathrm{ref}}-\boldsymbol{\Phi}\boldsymbol{w}\|_2^2+d} \tag{31}$$

根据前述的贝叶斯推理，我们可以通过式(26)、式(27)、式(29)、式(31)的迭代更新，当两次的迭代差值不超过10^{-3}，即可得到复激励权值$\boldsymbol{w}$，再根据复激励权值$\boldsymbol{w}$中非零元素的个数以及位置确定优化后的稀疏阵列中阵元的个数及位置。综上所述，近场稀疏阵列综合算法首先设置初始迭代次数、总迭代次数、收敛判断阈值和迭代变量的初始值，然后通过算法不断迭代更新，直到满足迭代收敛的阈值后得到复激励权值的最优值及其置信区间和置信度，实现复激励权值的可信推断。当稀疏阵列综合算法达到最大迭代次数时，输出的可能不是复激励权值的最优解，但它可以作为后续优化或进一步处理的起点，可以在此输出的基础上，通过调整算法参数、增加迭代次数来改善解的质量和收敛速度。稀疏阵列综合算法流程图如图4所示。

4 基于稀疏阵列改进三维时域成像算法

利用第3节所设计的近场稀疏阵列接收圆柱扫描所获得的人体实测回波数据后，由于对均匀阵列进行了稀疏综合，因此激励权值在阵列中不对称的分布，即某些阵元的权值较大，而其他阵元的权值较小，这将会导致目标散射点的点扩展函数旁瓣升高，图像出现散焦和伪影。通过基于稀疏阵列改进三维时域成像算法对距离向脉冲压缩后的回波数据进行稀疏恢复，实现近场稀疏阵列人体的三维恢复成像。首先在高度-距离维利用FFBP算法完成图像的聚焦。FFBP算法主要是通过孔径分解以及递归融合的方式进行成像，其处理过程如下[23]。

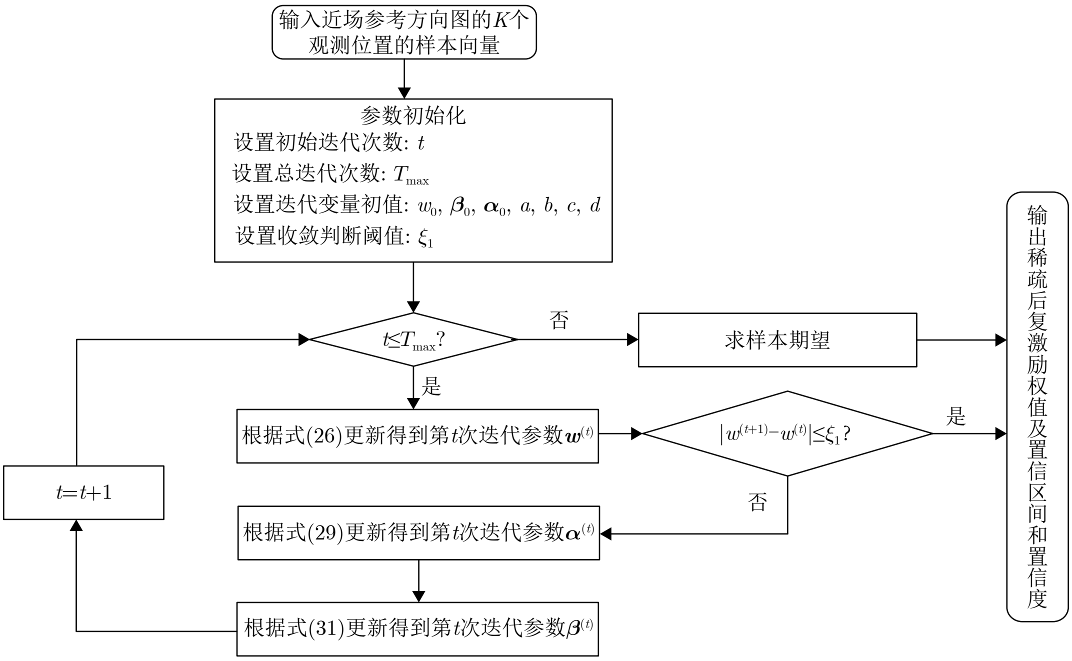

图 4 近场稀疏阵列综合算法流程图

Fig. 4 Flow chart of near-field sparse array synthesis algorithm

为了便于毫米波MIMO阵列的稀疏综合处理，基于等效相位中心近似来简化毫米波MIMO雷达信号模型，将多发多收的阵列结构转化为收发同置的均匀阵列，等效为它们中心位置的一个收发同置的相位中心。FFBP算法将整个等效相位中心孔径按照一定的分解系数划分成若干较短的子孔径，并将子孔径对应的距离压缩后的数据投影到以其孔径中心为原点的局部极坐标网格上面，从而得到粗角域分辨的子图像。由于初始阶段的子图像质量直接影响了后续图像融合的精度，因此在初始阶段的子孔径BP积分过程中需要引入积分孔径的判断。假设线性阵列孔径总长度$L_{\rm all}$，第$n(n=1,2,\cdots,N)$阶段的子孔径数目为$U^{(n)}=U^{(1)}/2^{n-1}$，每个子孔径的长度为$l^{(n)}=L_{\rm all}/U^{(n)}$，$\boldsymbol{w}=[w_1,w_2,\cdots,w_N]^{\rm T}$是$N$个阵元的复激励权值向量，$\boldsymbol{w}$中每一个元素都是由幅值和相位组成的，其中$\boldsymbol{w}$中每一个元素的位置代表着天线阵元的位置，每一个元素的大小代表着天线阵元激励的幅度，第$u(u=1,2,\cdots,U^{(n)})$个子孔径中心的高度坐标为$x_u^{(n)}=(u-U^{(n)}/2-1/2)\,l^{(n)}$，每个子孔径中含有的阵元数目$m$的大小取决于当前子孔径内稀疏的复激励权值向量$\boldsymbol{w}$的个数。每幅子孔径图像重建在各自的极坐标系下，本文以$\theta_u^{(n)}$表示第n阶段、第u个子孔径下的局部极坐标系的角域划分。如图5所示为第1阶段的第u个子孔径的局部极坐标网格。

如图5所示，对于第u个子孔径，以$x_u^{(1)}$为原点建立极坐标系$(\rho,\theta_u^{(1)})$，其中网格像素点P的极坐标为$(\rho,\theta_u^{(1)})$，阵元俯仰波束宽度为$\theta_{\rm beam}$，当阵元到网格像素点P的连线方向和视线方向的夹角φ不超过$\theta_{\rm beam}/2$时，阵元波束能够照射到P点，即

$$-\frac{\theta_{\rm beam}}{2}\le \arcsin\left[\frac{\left|\xi-\rho\sin\left(\theta_u^{(1)}\right)\right|}{R\left(\rho,\theta_u^{(1)};\xi\right)}\right]\le\frac{\theta_{\rm beam}}{2},\quad \xi\in\left[-\frac{l^{(1)}}{2},\frac{l^{(1)}}{2}\right] \tag{32}$$

本文将满足式(32)的ξ定义为像素点P的积分孔径，用符号$\xi^{\rm IA}$表示。对于第u个子孔径，如图5所示，则来自散射点P_0点处的回波数据为

$$S(t,\xi)=\sigma_i\sin{\rm c}\left(\frac{t-\dfrac{2R_0}{\rm c}}{T_{\rm p}}\right)\exp\left(-{\rm j}2\pi f_{\rm c}\frac{2R_0}{\rm c}\right) \tag{33}$$

其中，R_0为孔径位置ξ到目标点P_0的距离。当明确

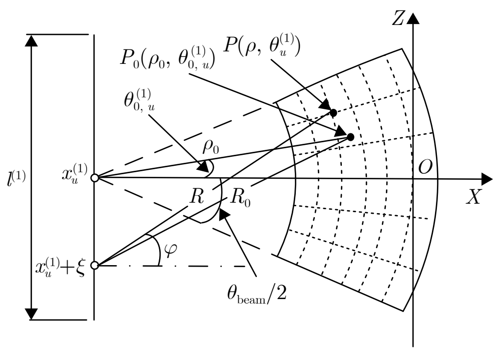

图 5 第1阶段的第u个子孔径的局部极坐标网格

Fig. 5 The first stage of the u subaperture of the local polar grid

知道成像网格上每个像素点的积分孔径时，第1阶段的第u个子孔径重建的图像表示为

$$I_u^{(1)}\left(\rho,\theta_u^{(1)}\right)=\int_{\xi\in\xi^{\mathrm{IA}}}S(t,\xi)\exp\left(\mathrm{j}K_{Rc}R(\rho,\theta_u^{(1)};\xi)\right)\mathrm{d}\xi \tag{34}$$

其中，$K_{Rc}=4\pi f_c/c$为中心频率波数，$R(\rho,\theta_u^{(1)};\xi)$为孔径位置$\xi$到网格像素点$P(\rho,\theta_u^{(1)})$的距离。

每个子孔径分别进行式(34)的积分处理，就可以获得第1阶段的子孔径下的高度-距离二维聚焦图像，此时得到的是粗角域的子图像。

其次是对先前阶段的子图像不断融合当前阶段的子图像，随着递归融合的不断进行，子孔径的长度不断增加，而子孔径的数目不断减少，子图像的分辨率不断提高，子孔径图像递归融合的表达式为

$$\begin{aligned}I_u^{(n)}\left(\rho,\theta_u^{(n)}\right)=\coprod\Big[&I_{2u-1}^{(n-1)}\left(\rho,\theta_{2u-1}^{(n-1)}\right)\\&+I_{2u}^{(n-1)}\left(\rho,\theta_{2u}^{(n-1)}\right)\Big],\\&\left\{\begin{array}{l}n=2,3,\cdots,N\\u=1,2,\cdots,U^{(n)}\end{array}\right.\end{aligned} \tag{35}$$

其中，$\coprod$表示相干相加。在完成最后一个阶段后，子孔径等于整个孔径，此时的局部极坐标等价于全局极坐标系。

最后，将极坐标图像$I(\rho,\theta)$变换到直角坐标系，得到全空间的分辨率图像$I(x,z)$。

经过以上FFBP处理后，高度-距离维实现了聚焦，而方位维的散射点仍然无法区分。由于BP成像算法具有较强的轨迹适应能力，能够在任意的非线性轨迹下实现对目标的聚焦，因此，利用BP算法进行方位-距离维的不同点目标的聚焦。首先需要将三维场景沿高度向划分为N个方位-距离维水平切面相叠加的形式，之后对每个切面进行网格点的划分，最后使用BP算法对每个水平切面进行二维成像，从而获得三维图像。

对于任意一个二维水平切面XOY，如图6所示，首先对每个方位时刻的一组距离向压缩数据进行插值，之后通过计算在旋转范围内阵元到网格上每一个点目标q的距离R_{ij}，根据R_{ij}找到坐标为(x_i,y_j)的点在二维数据中相对应的数值，在对相位补偿之后，将各个数值进行相干累加，得到该点的重建结果，即

$$I(x,y)=\int s_0(t,\theta)\exp(\mathrm{j}K_{Rc}R_{ij})\mathrm{d}y \tag{36}$$

其中，R_{ij}表示阵元到网格点的距离，$s_0(t,\theta)$表示距离-方位维的距离压缩数据。

以上完成了一个切面的处理，对于不同高度的水平切面XOY重复上述步骤，直到Z方向上所有切面完成二维成像，将高度-距离维的成像结果和方位-距离维的成像结果合并，即可得到最终目标的三维成像结果

$$I(x,y,z)=\{I(x,z),I(x,y)\} \tag{37}$$

最后，为了便于对场景目标的观察和检测，将重建的人体三维图像按照不同观测角度沿距离维进行最大值投影，即可得到不同角度观测下的二维人体图像。

5 实验验证

为了验证本文所提的可信推断近场稀疏综合阵列三维毫米波成像的有效性和优越性，设计了仿真模拟实验，与传统方法基于凸优化CVX求解的ℓ_1范数[24]和基于欠定系统局域解法(Focal Undetermined System Solver, FOCUSS)[25]合成稀疏阵列方向图对比，可信推断近场稀疏综合阵列提供了复激励权值$\boldsymbol{w}$的置信区间和置信度，并验证了在稀疏度、匹配性能的有效性和优越性，最后在相同的稀疏度情况下，基于设计的稀疏阵列采集近场一维电扫描圆周和二维平面全电扫实测回波数据后，验证了本文所提方法在保证成像结果的同时降低了系统的复杂度。

本节首先定义了稀疏度$\delta=M/M_{\mathrm{UNI}}$，$M$是非零激励权值$\boldsymbol{w}$的数量，$M_{\mathrm{UNI}}$是参考方向图均匀布局的阵列数目，参考方向图与合成方向图的归一化均方误差ε定义为

$$\varepsilon=\frac{\displaystyle\int|\boldsymbol{E}_{\mathrm{ref}}(\boldsymbol{r})-\boldsymbol{E}(\boldsymbol{r})|^2\mathrm{d}\boldsymbol{r}}{\displaystyle\int|\boldsymbol{E}_{\mathrm{ref}}(\boldsymbol{r})|^2\mathrm{d}\boldsymbol{r}} \tag{38}$$

其中，$\boldsymbol{E}(\boldsymbol{r})=\boldsymbol{\Phi}\boldsymbol{w_p}\in C^K$是最终稀疏阵列合成的方向图。式(38)可以清楚地看出合成方向图与参考方向图的均方误差与稀疏度成反比，我们的目标是使均方误差和稀疏度相平衡，也就是说在尽可能满足期望方向图性能的同时使得阵列中阵元的数量较

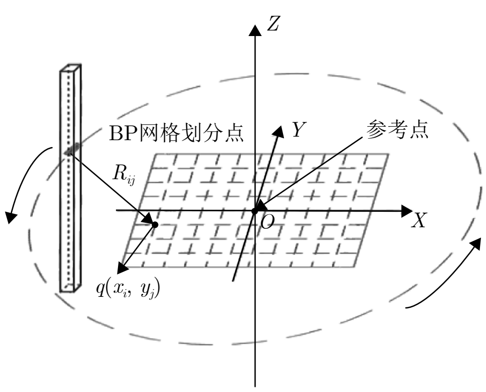

图 6 二维水平切面网格图

Fig. 6 Two-dimensional horizontal section grid diagram

少。然后，基于凸优化CVX求解的ℓ_1范数和基于FOCUSS法分别进行了稀疏阵列的合成，在达到同样的期望方向图性能时，对比了稀疏度和均方误差。最后，通过所设计的稀疏阵列接收人体的回波，利用改进三维时域成像算法对人体进行了三维重建[26]，从而验证所提算法在保证成像结果的同时降低了系统的复杂度的优势。

5.1　仿真模拟实验

本实验主要考虑一个近场低副瓣的参考方向图。生成该参考方向图的近场天线阵列的尺寸为191λ，采用单元间距为0.5λ的均匀线性阵列拓扑，阵元总数为383，设置近场聚焦线距离阵列的位置为0.628 m，其中，λ为0.01035 m，其采用了峰值旁瓣电平为–16 dB的泰勒分布参考方向图。阵列的参考点选择阵列的物理中心并将其作为坐标的原点$O(0,0)$。

图7中红色圆圈虚线代表参考方向图，蓝色星号点线分别代表本文所提算法，基于凸优化CVX求解的ℓ_1范数，基于FOCUSS法合成的稀疏阵列方向图，图7可以直观地看出本文所提方法与参考方向图更加接近，匹配性能更好。图8中红色圆圈虚线代表参考方向图的阵元位置及其幅值，蓝色星号点线分别代表本文所提算法，基于凸优化CVX求解的ℓ_1范数，基于FOCUSS法合成的稀疏阵列方向图的阵元位置及其幅值，图8可以看出本文所提方法相较于传统稀疏阵列合成方法相比，稀疏度更低，均匀布置的满阵中阵元稀疏的数量更多。为了对比不同位置聚焦线的聚焦效果，针对毫米波安检成像应用场景，人体目标距离阵列为0.4～0.8 m，

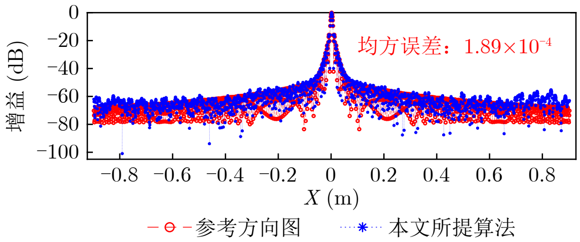

(a) 本文所提算法合成的方向图与参考方向图
(a) The pattern and reference pattern synthesized by the proposed algorithm

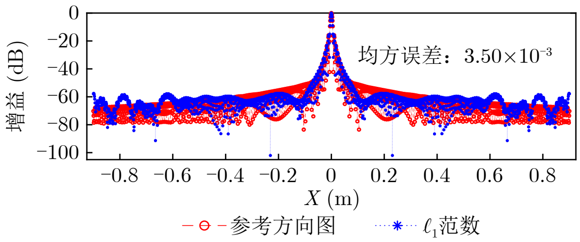

(b) 基于凸优化CVX求解的ℓ_1范数合成的方向图与参考方向图
(b) The pattern and reference pattern synthesized by the ℓ_1 norm solved by convex optimization CVX

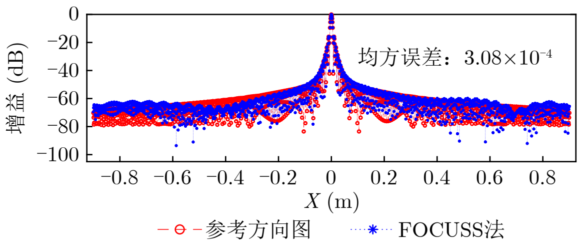

(c) 基于FOCUSS法合成的方向图与参考方向图
(c) The pattern and reference pattern synthesized by FOCUSS method

图 7 不同算法下的近场天线方向图

Fig. 7 The direction pattern of near-field antenna and the position and amplitude of near-field array under different algorithms

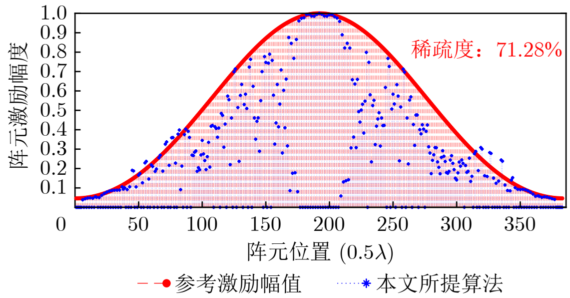

(a) 本文所提算法合成方向图与参考方向图的阵元位置及幅值
(a) The proposed algorithm synthesizes element positions and amplitudes of the pattern and reference pattern

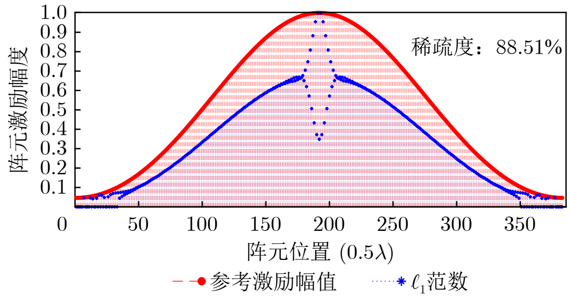

(b) 基于凸优化CVX求解的ℓ_1范数合成方向图与参考方向图的阵元位置及幅值
(b) The ℓ_1 norm synthesizes element positions and amplitudes of the pattern and reference pattern based on convex optimization CVX solution

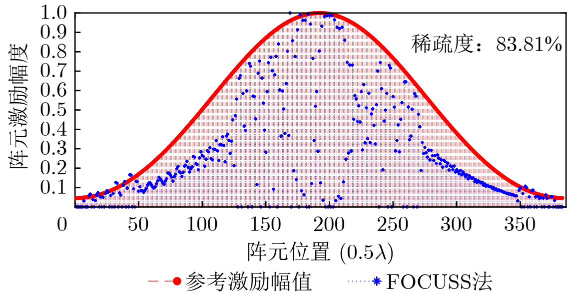

(c) 基于FOCUSS法合成方向图与参考方向图的阵元位置及幅值
(c) The synthesizes element positions and amplitudes of the pattern and reference pattern based on FOCUSS method

图 8 不同算法下的近场阵元位置及其幅度

Fig. 8 The position and amplitude of near-field array under different algorithms

因此设置近场聚焦线为0.4 m, 0.5 m, 0.6 m, 0.7 m, 0.8 m，不同聚焦线位置的匹配参考方向图的均方误差如图9所示，可以看出本文所提稀疏阵列综合算法匹配参考方向图的均方误差最小。

从表1的数据中可以定量看出，在满足参考方向图性能彼此相差无几时，可以明显地看出本文所提出的算法与其他稀疏阵列合成算法相比，可以稀疏110个阵元，稀疏度为71.28%，稀疏阵列合成的方向图与参考方向图的归一化均方误差为1.89×10^{-4}，而基于凸优化CVX求解的ℓ_1范数稀疏阵列合成算法稀疏44个阵元，稀疏度为88.51%，均方误差为3.50×10^{-3}，基于FOCUSS方法的稀疏阵列合成算法稀疏62个阵元，稀疏度为83.81%，均方误差为3.08×10^{-4}。定量分析可看出本文所提算法匹配参考方向图的精度更好，稀疏度更低，阵列成本及其系统馈电网络复杂度可以设计地更低。

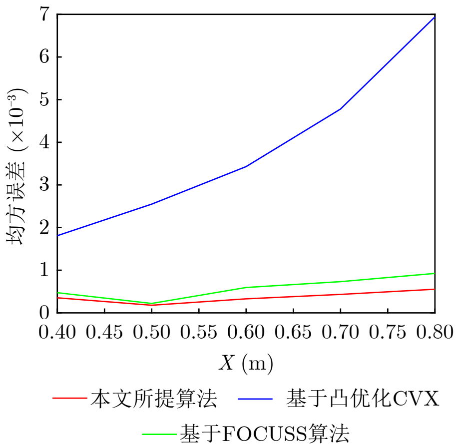

图 9 不同聚集线位置下不同算法匹配参考方向图的均方误差对比图

Fig. 9 Different algorithms match the mean square error comparison graph of reference direction graph under different aggregation line positions

在稀疏贝叶斯学习的框架下，利用本文所提出的算法求得复激励权值解析的后验概率密度函数，从而获得高阶统计信息，进而得到了复激励权值的期望及方差。在稀疏阵列综合后的方向图与参考方向图均方误差在1.89×10^{-4}的情况下，根据设置的显著性水平为0.05，可以确定每个阵元的幅度最大不会超过置信区间上限，最小不会低于置信区间下限时，可以满足方向图的匹配性能，为现实应用中激励幅值的评估提供了边界判定依据。但是如果直接将置信区间下限小于零的阵元置零，虽然提高了稀疏性，但是匹配精度将会严重下降。其中图10为近场阵元位置及其激励权值幅度的置信区间图，其中蓝色代表激励权值幅度(期望)，红色代表激励权值在置信度为95%下的置信区间。

5.2 稀疏阵列重建图像实测数据验证

为了验证5.1节所合成的稀疏阵列的可行性、适用性及所提算法的高精度的优势，本节采用机械和电扫描相结合圆周实测数据和二维全电扫面阵实测数据进行实验验证。机械和电扫描相结合圆周成像系统采用的是以固定的角速度沿圆周运动的线性

表 1 不同稀疏阵列合成算法下的性能对比

Tab. 1 Performance comparison of different sparse array synthesis algorithms

方法	峰值旁瓣电平(dB)	阵元个数	稀疏度(%)	均方误差
本文所提方法	–15.81	273	71.28	1.89×10^{-4}
ℓ_1范数	–15.76	339	88.51	3.50×10^{-3}
FOCUSS法	–15.68	321	83.81	3.08×10^{-4}

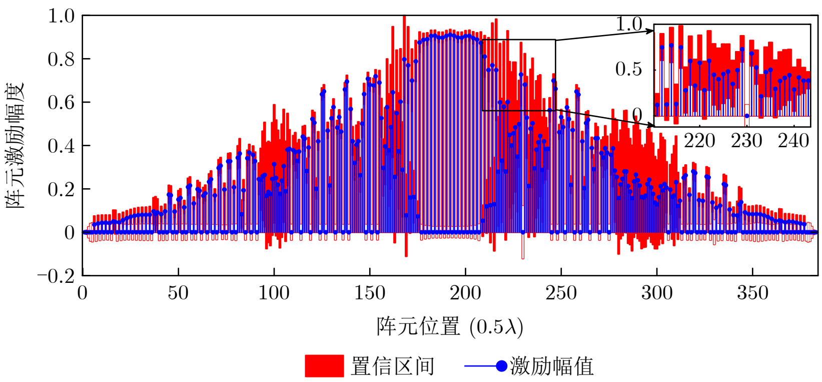

图 10 近场阵元位置及幅度的置信区间

Fig. 10 Confidence interval for the position and amplitude of near-field elements

阵列，围绕实测人体进行圆周柱面扫描接收人体的回波，毫米波电扫描圆周成像系统相关参数如表2所示。二维全电扫面阵成像系统采用480×480阵元的二维平面阵，天线阵大小为1.0 m×1.8 m，阵元之间的间距为12.6 mm，平面阵离中心点距离为0.85 m，系统工作频率为27 GHz，系统工作带宽为6.5 GHz，对实测人体进行快拍接收人体回波。

为了定性比较稀疏阵列综合后成像的效果，以本文所提算法稀疏度为基准，将基于凸优化CVX求解的ℓ_1范数得到的最优复激励权值小于等于一个阈值进行归零，使得稀疏优化掉与本文所提算法相同的阵元个数。同样，将基于FOCUSS方法得到的最优复激励权值小于等于一个阈值进行归零，使得稀疏优化掉与本文所提算法相同的阵元个数，至此得到相同的稀疏度71.28%。图11(a)所示成像结果为通过圆周线性阵列扫描采集得到回波数据后完成三维成像处理后沿距离维最大值投影得到的成像图，图11(b)、图11(c)、图11(d)分别为在相同的稀疏度71.28%情况下，本文所提算法设计的稀疏阵列，基于凸优化CVX求解的ℓ_1范数所设计的稀疏阵列，基于FOCUSS方法所设计的稀疏阵列，分别利用所设计的稀疏阵列采集得到人体的回波，通过改进三维时域成像算法完成三维重建，沿距离维最大值投影得到的成像图。图12(a)所示成像结果为通过二维全电扫面阵采集得到回波数据后完成三维成像处理后沿距离维最大值投影得到的成像图，图12(b)、图12(c)、图12(d)分别为在相同的稀疏度64.67%情况下，本文所提算法设计的稀疏阵列，基于凸优化CVX求解的ℓ_1范数所设计的稀疏阵列，基于FOCUSS方法所设计的稀疏阵列，分别利用所设计的稀疏阵列采集得到人体的回波，通过改进三维时域成像算法完成三维重建，沿距离维最大值投影得到的成像图。为了全方位地比较成像效果，在相同的稀疏度71.28%情况下，方位15°时不同方法设计的圆周线性稀疏阵列侧面成像结果如图13所示，图13(a)、图13(b)、图13(c)、图13(d)分别为在方位15°时，均匀阵列成像，本文所提算法设计的稀疏阵列成像

表 2　毫米波电扫描圆周成像系统相关参数

Tab. 2　Parameters of milli-meter wave electrical scanning circumferential imaging system

参数	数值
系统工作带宽	6.5 GHz
工作频率	27 GHz
目标距离	0.4～0.8 m
方位/俯仰角	55°/55°
采样点数	64
阵元间距	0.0052 m
旋转次数	314
单次旋转角度	0.2867°
旋转半径	0.628 m

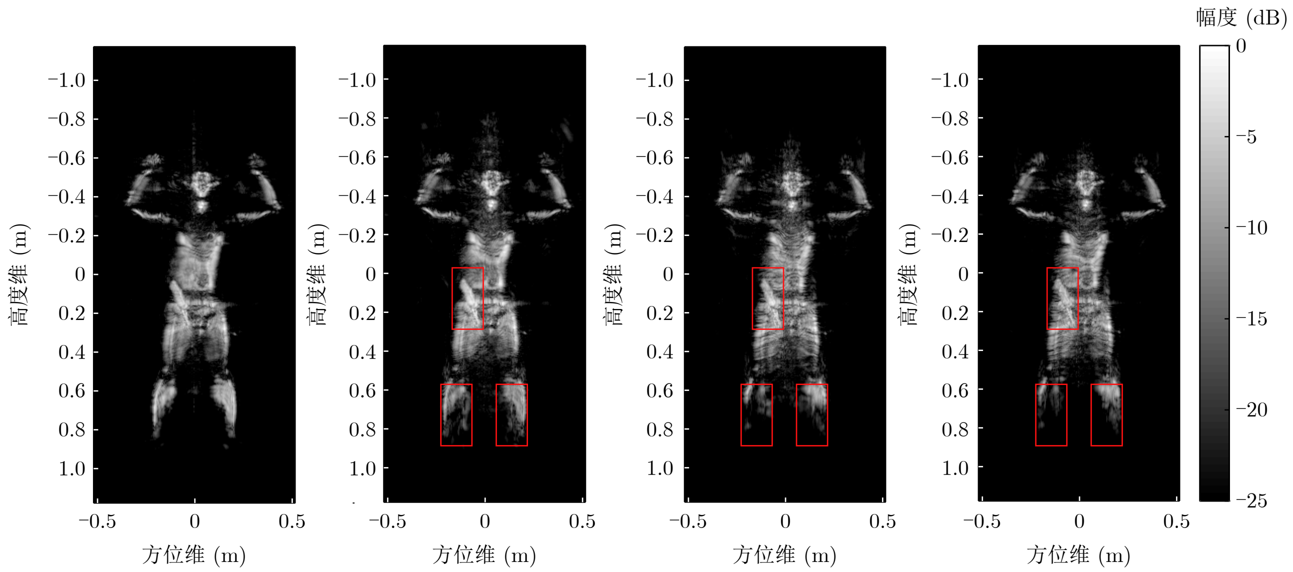

(a) 均匀阵列成像

(a) Uniform array imaging

(b) 本文所提算法设计的稀疏阵列成像结果

(b) Sparse array imaging results designed by the algorithm proposed in this paper

(c) 基于凸优化CVX求解的ℓ_1范数设计的稀疏阵列成像结果

(c) Sparse array imaging results designed based on the ℓ_1 norm solved by CVX

(d) FOCUSS方法所设计的稀疏阵列成像结果

(d) Sparse array imaging results designed by FOCUSS method

图 11 相同稀疏度下不同方法设计的圆周线性稀疏阵列获得的成像结果对比

Fig. 11 Comparison of imaging results obtained by circular linear sparse arrays designed by different methods under the same sparsity

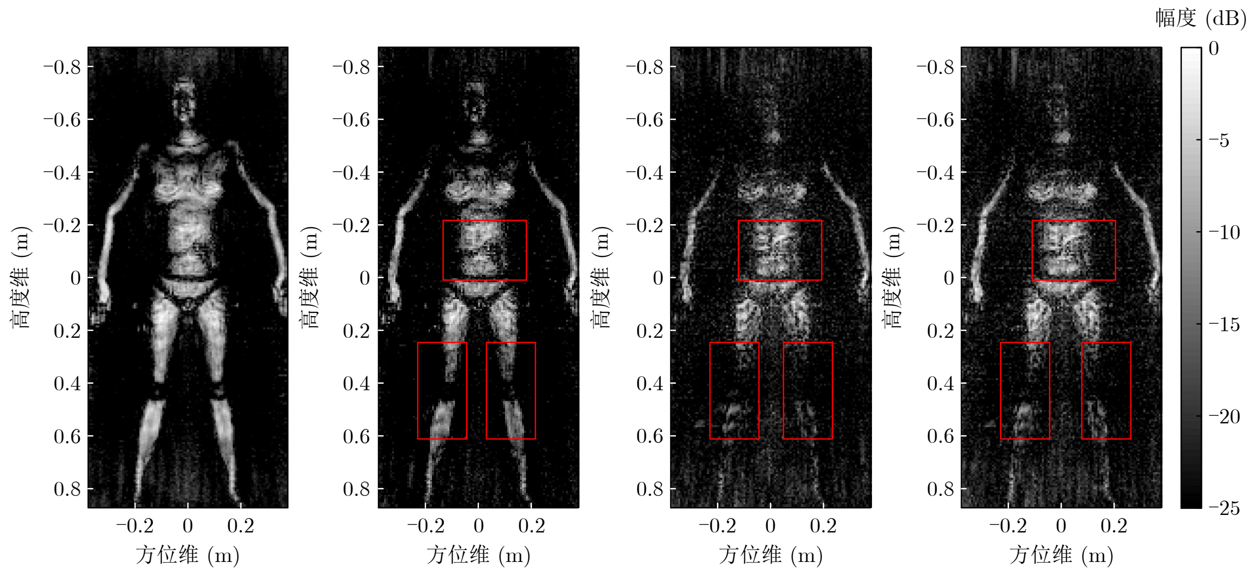

(a) 均匀面阵成像

(a) Uniform planar array imaging

(b) 本文所提算法设计的稀疏阵列成像结果

(b) Sparse array imaging results designed by the algorithm proposed in this paper

(c) 基于凸优化CVX求解的ℓ_1范数设计的稀疏阵列成像结果

(c) Sparse array imaging results designed based on the ℓ_1 norm solved by CVX

(d) FOCUSS方法所设计的稀疏阵列成像结果

(d) Sparse array imaging results designed by FOCUSS method

图 12 相同稀疏度下不同方法设计的全电扫平面稀疏阵列获得的成像结果对比

Fig. 12 Comparison of imaging reaults obtained by full scanned planar sparse arrays designed by different methods under the same sparsity

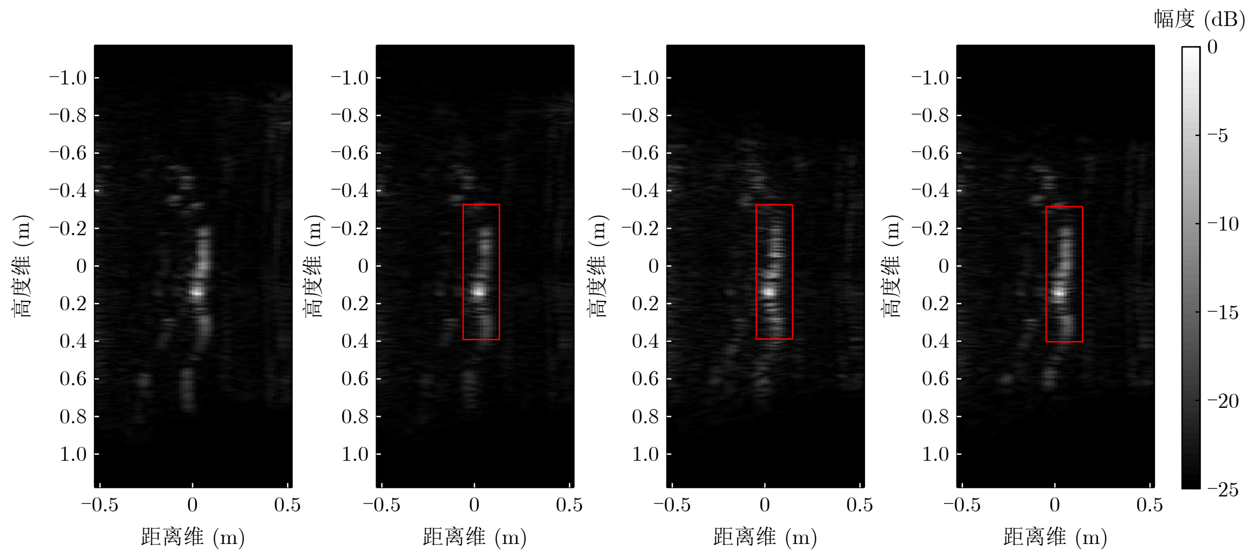

(a) 均匀阵列成像

(a) Uniform array imaging

(b) 本文所提算法设计的稀疏阵列成像结果

(b) Sparse array imaging results designed by the algorithm proposed in this paper

(c) 基于凸优化CVX求解的ℓ_1范数设计的稀疏阵列成像结果

(c) Sparse array imaging results designed based on the ℓ_1 norm solved by CVX

(d) FOCUSS方法所设计的稀疏阵列成像结果

(d) Sparse array imaging results designed by FOCUSS method

图 13 方位15°时不同方法设计的圆周线性稀疏阵列侧面成像结果对比

Fig. 13 Comparison of side imaging results of circular linear sparse array designed by different methods at 15° orientation

结果，基于凸优化CVX求解的ℓ_1范数设计的稀疏阵列成像结果，基于FOCUSS方法设计的稀疏阵列成像结果，可以看出图13(b)相对于图13(c)、图13(d)，红框示例区域聚焦效果相对良好。

从定性的角度来说，在相同的稀疏度情况下，分别对比图11(b)、图11(c)、图11(d)和图12(b)、图12(c)、图12(d)的结果可以发现，图11(c)、图11(d)和图12(c)、图12(d)在人体容易藏匿危险品的位置，如左、右大腿和小腿，前腰、胳膊和前胸的位置成像对比度差，成像结果特征丢失严重，影响危

险品的检测，使得安检系统难以在实际场合中应用。而图11(b)相较于图11(c)和图11(d)，图12(b)相较于图12(c)和图12(d)的成像结果，人体主要藏匿危险品的位置成像清晰，关节分明，聚焦效果较好。但是图11(a)成像的数据量为64×383×314，而图11(b)成像的数据量为64×273×314，图12(a)的成像数据量为64×480×480，而图12(b)的成像数据量为64×386×386，相较于图11和图12(a)，图11和图12(b)的结果显示利用本文所提方法进行稀疏阵列成像可以在保证成像质量的同时，使得成像数据量分别减少了28.72%和35.33%，且FFBP算法的运算复杂度为$O(N^2\log_2 N)$，BP算法运算复杂度为$O(N^3)$，计算平台是基于Windows 10个人计算机上的Matlab 2018b进行(Intel(R)Core(TM)i5-9300H CPU @ 2.40 GHz, 16GB RAM)，FFBP算法耗时863 s，BP算法耗时33752 s。故本文所提的高稀疏可信推断近场稀疏综合阵列三维成像算法可以在保证成像质量接近均匀阵列参考成像结果的同时，降低系统馈电网络的复杂度。

从定量的角度分析，开展点目标仿真模拟试验，如图14所示，我们选取3×3×3的散射点集合，每个点间的各向距离均为0.2 m，构成尺寸大小为

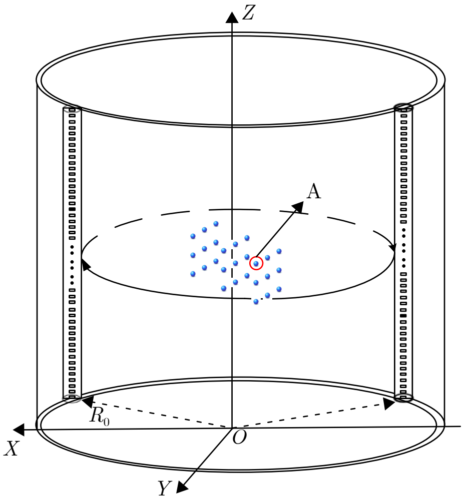

图 14 边缘点A的位置示意图

Fig. 14 Diagram of the position of edge point A

0.4 m×0.4 m×0.4 m，反射系数均为常数的27点模拟立方模型，选取立方模型的一个边缘点目标A，分析其聚焦性能，对其分别利用均匀阵列、本文所提算法稀疏阵列、基于FOCUSS算法稀疏阵列、基于凸优化CVX求解的ℓ_1范数稀疏阵列进行成像，给出方位向及高度向剖面图，定量分析其成像聚焦性能，实验结果如图15所示。由图15和表3可以看

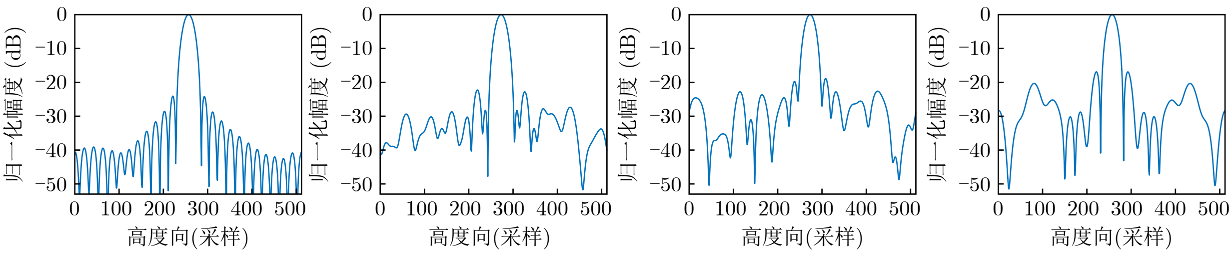

(a) 均匀阵列成像边缘点A的高度剖面图
(a) Height profile of edge point A of uniform array imaging

(b) 本文所提算法稀疏阵列成像边缘点A的高度剖面图
(b) Height profile of image edge point A of sparse arry based on the algorithm proposed in tis pape

(c) 基于FOCUSS算法稀疏阵列成像边缘点A的高度剖面图
(c) Height profile of image edge point A of sparse array based on FOCUSS algorithm

(d) 基于凸优化CVX求解的ℓ_1范数稀疏阵列成像边缘点A的高度剖面图
(d) Height profile of image edge point A of ℓ_1 norm sparse array based on convex optimization CVX solutiond

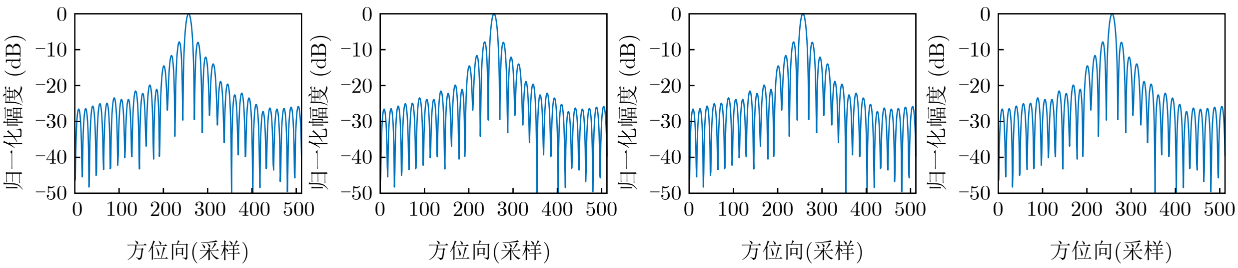

(e) 均匀阵列成像边缘点A的方位剖面图
(e) Azimuth profile of edge point A of uniform array imaging

(f) 本文所提算法稀疏阵列成像边缘点A的方位剖面图
(f) Azimuth profile of image edge point A by sparse array based on the algorithm proposed in this paper

(g) 基于FOCUSS算法稀疏阵列成像边缘点A的方位剖面图
(g) Azimuth profile of image edge point A of sparse array based on FOCUSS algorithm

(h) 基于凸优化CVX求解的ℓ_1范数稀疏阵列成像边缘点A的方位剖面图
(h) Azimuth profile of image edge point A of ℓ_1 norm sparse array based on convex optimization CVX solutionh

图 15 不同稀疏阵列综合算法成像结果边缘点的剖面图

Fig. 15 Profile of edge points of imaging results of different sparse array synthesis algorithms

表 3 不同稀疏阵列综合方法成像结果边缘点的剖面图定量分析

Tab. 3 Quantitative analysis of profile of edge points of imaging results by different sparse array synthesis methods

边缘点的成像结果	高度向峰值旁瓣比(dB)	3 dB宽度时高度向分辨率(mm)	方位向峰值旁瓣比(dB)	3 dB宽度时方位向分辨率(mm)
均匀阵列成像	–24.69	7.76	–8.01	4.2
本文所提算法稀疏阵列成像	–22.15	7.76	–8.01	4.2
基于FOCUSS算法稀疏阵列成像	–20.18	7.79	–8.01	4.2
基于凸优化CVX求解的ℓ_1范数稀疏阵列成像	–17.98	7.82	–8.01	4.2

出，在方位向，由于未进行稀疏综合处理，均匀阵列、本文所提算法稀疏阵列、基于FOCUSS算法稀疏阵列、基于凸优化CVX求解的ℓ_1范数稀疏阵列成像剖面图具有相同的峰值旁瓣比和分辨率，具有相同的成像质量，在高度向，可以看出本文所提算法稀疏阵列相比于FOCUSS算法稀疏阵列、凸优化CVX求解的ℓ_1范数稀疏阵列峰值旁瓣电平更低，分辨率更高，但是相比于均匀阵列峰值旁瓣电平从–24.69 dB升高到–22.15 dB，升高了2.54 dB，成像质量下降，但是在阵列成本及馈电网络复杂度显著降低的情况下，高度向成像质量的些许下降在可接受的范围内。

6 结语

本文针对毫米波主动式电扫描成像系统面临着系统成本、成像精度和成像速度之间的矛盾，提出了可信推断近场稀疏综合阵列三维毫米波成像算法，用于设计满足期望方向图的近场稀疏阵列，并结合改进三维时域成像算法进行重建以此来验证在系统低成本和复杂度下，实现高精度的成像。在稀疏贝叶斯学习框架下，将近场稀疏阵列综合问题建模为贝叶斯压缩感知问题，利用参考方向图和误差变量进行概率与统计建模，并对复激励权值进行分层建模，通过变分贝叶斯期望最大化算法获取了解析的复激励权值的后验概率密度函数，从而获得了高阶统计信息，进一步获得了复激励权值的最优值及其动态范围，实现了复激励权值的动态指示。通过本文算法所设计的稀疏阵列与现有的稀疏阵列合成技术相比较，证明了本文所提算法在稀疏度和匹配精度方面的有效性和优越性，相较于均匀间隔布局的阵列，本文所设计的稀疏阵列可以减少29%左右的阵元数量。最后基于一维电扫圆周和二维平面全电扫实测数据，利用改进三维时域成像算法进行三维重建，验证了所提算法保证成像结果的同时降低了系统复杂性的优势。

利益冲突 所有作者均声明不存在利益冲突

Conflict of Interests The authors declare that there is no conflict of interests

参 考 文 献

[1] 马宇欣, 海宇, 李中余, 等. 稀疏轨迹毫米波雷达三维高分辨成像算法[J]. 雷达学报, 2023, 12(5): 1000–1013. doi: 10.12000/JR23001.

MA Yuxin, HAI Yu, LI Zhongyu, *et al*. 3D high-resolution imaging algorithm with sparse trajectory for millimeter-wave radar[J]. *Journal of Radars*, 2023, 12(5): 1000–1013. doi: 10.12000/JR23001.

[2] MA Zhaohui, WANG Jingyang, JING Handan, *et al*. Millimeter wave security imaging based on single-channel MIMO radar[J]. *Journal of Infrared and Millimeter Waves*, 2020, 39(6): 709–717. doi: 10.11972/j.issn.1001-9014.2020.06.008.

[3] 刘可, 朱泽政, 于军, 等. 基于互质阵列孔洞分析的稀疏阵列设计方法[J]. 电子与信息学报, 2022, 44(1): 372–379. doi: 10.11999/JEIT201024.

LIU Ke, ZHU Zezheng, YU Jun, *et al*. Sparse array design methods based on hole analysis of the coprime array[J]. *Journal of Electronics & Information Technology*, 2022, 44(1): 372–379. doi: 10.11999/JEIT201024.

[4] KARIMKASHI S and KISHK A A. Focused microstrip array antenna using a Dolph-Chebyshev near-field design[J]. *IEEE Transactions on Antennas and Propagation*, 2009, 57(12): 3813–3820. doi: 10.1109/TAP.2009.2033435.

[5] 赵磊, 黄昆, 郝鑫, 等. 近场雷达成像非均匀稀疏阵设计[J]. 太赫兹科学与电子信息学报, 2017, 15(5): 707–710. doi: 10.11805/TKYDA201705.0707.

ZHAO Lei, HUANG Kun, HAO Xin, *et al*. Non-uniform sparse array design in near field radar imaging[J]. *Journal of Terahertz Science and Electronic Information Technology*, 2017, 15(5): 707–710. doi: 10.11805/TKYDA201705.0707.

[6] ZHAO Dongdong, LIU Xuesong, CHEN Wenyuan, *et al*. Optimized design for sparse cross arrays in both near-field and far-field[J]. *IEEE Journal of Oceanic Engineering*, 2019, 44(3): 783–795. doi: 10.1109/JOE.2018.2837458.

[7] LEMAITRE-AUGER P, ABIELMONA S, and CALOZ C. Generation of Bessel beams by two-dimensional antenna arrays using sub-sampled distributions[J]. *IEEE*

Transactions on Antennas and Propagation, 2013, 61(4): 1838–1849. doi: 10.1109/TAP.2012.2232263.

[8] LI Pengfa, QU Shiwei, YANG Shiwen, *et al*. Focused array antenna based on subarrays[J]. *IEEE Antennas and Wireless Propagation Letters*, 2017, 16: 888–891. doi: 10.1109/LAWP.2016.2613887.

[9] RUDOLPH D L and BAROTT W C. Reduction of near-field grating lobes in sparse linear phased arrays[C]. 2014 IEEE Antennas and Propagation Society International Symposium, Memphis, USA, 2014: 1155–1156. doi: 10.1109/APS.2014.6904904.

[10] OLIVERI G and MASSA A. Bayesian compressive sampling for pattern synthesis with maximally sparse non-uniform linear arrays[J]. *IEEE Transactions on Antennas and Propagation*, 2011, 59(2): 467–481. doi: 10.1109/TAP.2010.2096400.

[11] OLIVERI G, CARLIN M, and MASSA A. Complex-weight sparse linear array synthesis by Bayesian compressive sampling[J]. *IEEE Transactions on Antennas and Propagation*, 2012, 60(5): 2309–2326. doi: 10.1109/TAP.2012.2189742.

[12] 杨磊, 陈英杰, 王腾腾, 等. 旅客人身时频调和型毫米波三维重建[J]. 红外与毫米波学报, 2023, 42(3): 327–338. doi: 10.11972/j.issn.1001-9014.2023.03.006.

YANG Lei, CHEN Yingjie, WANG Tengteng, *et al*. Three-dimensional reconstruction algorithm for passengers based on time-frequency coordination[J]. *Journal of Infrared and Millimeter Waves*, 2023, 42(3): 327–338. doi: 10.11972/j.issn.1001-9014.2023.03.006.

[13] 陈秀琴, 李跃华, 孔令雄. 毫米波近场成像及图像增强算法研究[J]. 微波学报, 2023, 39(S1): 324–327.

CHEN Xiuqin, LI Yuehua, and KONG Lingxiong. Research on millimeter wave near field imaging and image enhancement algorithms[J]. *Journal of Microwaves*, 2023, 39(S1): 324–327.

[14] 谢朋飞, 张磊, 吴振华. 融合ω-K和BP算法的圆柱扫描毫米波三维成像算法[J]. 雷达学报, 2018, 7(3): 387–394. doi: 10.12000/JR17112.

XIE Pengfei, ZHANG Lei, and WU Zhenhua. A three-dimensional imaging algorithm fusion with ω-K and BP algorithm for millimeter-wave cylindrical scanning[J]. *Journal of Radars*, 2018, 7(3): 387–394. doi: 10.12000/JR17112.

[15] LIN Zhenwei, CHEN Yaowu, LIU Xuesong, *et al*. Optimized design for sparse arrays in 3-D imaging sonar systems based on perturbed Bayesian compressive sensing[J]. *IEEE Sensors Journal*, 2020, 20(10): 5554–5565. doi: 10.1109/JSEN.2020.2971568.

[16] 宋嘉奇, 陶海红. 一种稀布阵列天线的近场波束综合算法[J]. 西安电子科技大学学报: 自然科学版, 2018, 45(6): 14–18. doi: 10.3969/j.issn.1001-2400.2018.06.003.

SONG Jiaqi and TAO Haihong. Near-field beam synthesis algorithm for sparse array antennas[J]. *Journal of Xidian University: Natural Science*, 2018, 45(6): 14–18. doi: 10.3969/j.issn.1001-2400.2018.06.003.

[17] HUANG Zixuan and CHENG Yujian. Near-field pattern synthesis for sparse focusing antenna arrays based on Bayesian compressive sensing and convex optimization[J]. *IEEE Transactions on Antennas and Propagation*, 2018, 66(10): 5249–5257. doi: 10.1109/TAP.2018.2860044.

[18] KIM S, DONG H J, YU J W, *et al*. Phased array calibration system with high accuracy and low complexity[J]. *Alexandria Engineering Journal*, 2023, 69: 759–770. doi: 10.1016/j.aej.2023.02.026.

[19] 祁峥东, 卢阳沂, 孔玥, 等. 基于多凸优化的稀疏线性阵列综合方法[J]. 雷达与对抗, 2019, 39(4): 21–24, 49. doi: 10.19341/j.cnki.issn.1009-0401.2019.04.006.

QI Zhengdong, LU Yangyi, KONG Yue, *et al*. Synthesis of sparse linear arrays based on multi-convex optimization[J]. *Radar & ECM*, 2019, 39(4): 21–24, 49. doi: 10.19341/j.cnki.issn.1009-0401.2019.04.006.

[20] BABACAN S D, MOLINA R, and KATSAGGELOS A K. Bayesian compressive sensing using Laplace priors[J]. *IEEE Transactions on Image Processing*, 2010, 19(1): 53–63. doi: 10.1109/TIP.2009.2032894.

[21] LIU Ying, ZHANG Zongyu, ZHOU Chengwei, *et al*. Robust variational Bayesian inference for direction-of-arrival estimation with sparse array[J]. *IEEE Transactions on Vehicular Technology*, 2022, 71(8): 8591–8602. doi: 10.1109/TVT.2022.3173418.

[22] ZHAO Xiaowen, YANG Qingshan, and ZHANG Yunhua. A hybrid method for the optimal synthesis of 3-D patterns of sparse concentric ring arrays[J]. *IEEE Transactions on Antennas and Propagation*, 2016, 64(2): 515–524. doi: 10.1109/TAP.2015.2504377.

[23] 李浩林, 陈露露, 张磊, 等. 快速分解后向投影SAR成像的自聚焦算法研究[J]. 电子与信息学报, 2014, 36(4): 938–945. doi: 10.3724/SP.J.1146.2013.00011.

LI Haolin, CHEN Lulu, ZHANG Lei, *et al*. Study of autofocus method for SAR imagery created by fast factorized backprojection[J]. *Journal of Electronics & Information Technology*, 2014, 36(4): 938–945. doi: 10.3724/SP.J.1146.2013.00011.

[24] MA Chengzheng, YEO T S, LIU Zhoufeng, *et al*. Target imaging based on ℓ1ℓ0 norms homotopy sparse signal recovery and distributed MIMO antennas[J]. *IEEE Transactions on Aerospace and Electronic Systems*, 2015, 51(4): 3399–3414. doi: 10.1109/TAES.2015.140939.

[25] 杨鹏, 闫飞, 张胜辉, 等. 基于FOCUSS算法的稀疏阵列综合[J]. 电子科技大学学报, 2014, 43(2): 203–206. doi: 10.3969/j.issn.1001-0548.2014.02.008.

YANG Peng, YAN Fei, ZHANG Shenghui, *et al*. Sparse array synthesis based on FOCUSS algorithm[J]. *Journal of University of Electronic Science and Technology of China*, 2014, 43(2): 203–206. doi: 10.3969/j.issn.1001-0548.2014.02.008.

[26] 邢孟道, 马鹏辉, 楼屹杉, 等. 合成孔径雷达快速后向投影算法综述[J]. 雷达学报, 2024, 13(1): 1–22. doi: 10.12000/JR23183.

XING Mengdao, MA Penghui, LOU Yishan, *et al*. Review of fast back projection algorithmsin synthetic aperture radar[J]. *Journal of Radars*, 2024, 13(1): 1–22. doi: 10.12000/JR23183.

作 者 简 介

杨　磊，博士，教授，博士生导师，主要研究方向为高分辨SAR成像及机器学习理论应用。

霍　鑫，博士生，主要研究方向为毫米波成像与稀疏阵列构型设计。

申瑞阳，硕士生，主要研究方向为毫米波成像与稀疏阵列构型设计。

宋　昊，硕士生，主要研究方向为毫米波成像与稀疏阵列构型设计。

胡仲伟，博士，讲师，硕士生导师，主要研究方向为高分辨SAR成像及优化学习理论。

(责任编辑：于青)

Credible Inference of Near-field Sparse Array Synthesis for Three-dimensional Millimeter-wave Imagery

YANG Lei* HUO Xin SHEN Ruiyang SONG Hao HU Zhongwei*

(*College of Electronic Information and Automation*, *Civil Aviation University of China*, *Tianjin* 300300, *China*)

Abstract: Due to the short wavelength of millimeter-wave, active electrical scanning millimeter-wave imaging system requires large imaging scenarios and high resolutions in practical applications. These requirements lead to a large uniform array size and high complexity of the feed network that satisfies the Nyquist sampling theorem. Accordingly, the system faces contradictions among imaging accuracy, imaging speed, and system cost. To this end, a novel, Credible Bayesian Inference of near-field Sparse Array Synthesis (CBI-SAS) algorithm is proposed under the framework of sparse Bayesian learning. The algorithm optimizes the complex-valued excitation weights based on Bayesian inference in a sparse manner. Therefore, it obtains the full statistical posterior Probability Density Function (PDF) of these weights. This enables the algorithm to utilize higher-order statistical information to obtain the optimal values, confidence intervals, and confidence levels of the excitation weights. In Bayesian inference, to achieve a small number of array elements to synthesize the desired beam orientation pattern, a heavy-tailed Laplace sparse prior is introduced to the excitation weights. However, considering that the prior probability model is not conjugated with the reference pattern data probability, the prior model is encoded in a hierarchical Bayesian manner so that the full posterior distribution can be represented in closed-form solutions. To avoid the high-dimensional integral in the full posterior distribution, a variational Bayesian expectation maximization method is employed to calculate the posterior PDF of the excitation weights, enabling reliable Bayesian inference. Simulation results show that compared with conventional sparse array synthesis algorithms, the proposed algorithm achieves lower element sparsity, a smaller normalized mean square error, and higher accuracy for matching the desired directional pattern. In addition, based on the measured raw data from near-field 1D electrical scanning and 2D plane electrical scanning, an improved 3D time domain algorithm is applied for 3D image reconstruction. Results verify that the proposed CBI-SAS algorithm can guarantee imaging results and reduce the complexity of the system.

Key words: Millimeter-wave imagery; Bayesian inference; Sparse array synthesis; Hierarchical Bayesian; Variational Bayesian expectation maximization

CLC index: TN957 **Document code**: A **Article number**: 2095-283X(2024)05-1092-21

DOI: 10.12000/JR24097

Reference format: YANG Lei, HUO Xin, SHEN Ruiyang, *et al*. Credible inference of near-field sparse array synthesis for three-dimensional millimeter-wave imagery[J]. *Journal of Radars*, 2024, 13(5): 1092–1112. DOI: 10.12000/JR24097.

1 Introduction

In recent years, terrorist activities have frequently occurred internationally, posing challenges to the development and stability of human society. Therefore, higher requirements have been put forward for security equipment in places with high traffic, such as civil airports, bus terminals, and train stations. Traditional security inspection equipment includes handheld metal detectors, X-ray security inspection machines, and so on. Among them, handheld metal detectors can detect metallic dangerous goods, but are ineffective for non-metallic sones, and their detection range is limited, resulting in low detection efficiency[1]. The X-ray security inspection machine is superi-

Manuscript received May 22, 2024; Revised August 05, 2024; Published online August 26, 2024

*Corresponding Authors: HU Zhongwei, zwhu@cauc.edu.cn; YANG Lei, yanglei840626@163.com

Foundation Items: The National Natural Science Foundation of China (62271487), Fundamental Research Funds for the Central Universities (3122023PT04)

Corresponding Editor: DENG Bin

or to metal detectors in terms of detection efficiency and accuracy, but the ionization of X-rays can cause radiation damage to human health and is not suitable for security inspection. With the rapid development of millimeter-wave devices and integrated circuit technology, security inspection technology based on millimeter-wave three-dimensional (3D) imaging has become a research hotspot. The frequency band of millimeter-waves is between 30—300 GHz, and the wavelength is in the range of 1—10 mm. It can easily penetrate the surface clothing of the human body to detect hidden dangerous goods without the blackbody effect, and it will not cause radiation accumulation in the human body[2]. However, in actual security check situations, it is necessary to cover a large imaging range and achieve high imaging resolution. However, the wavelength of millimeter waves is relatively short, and for a uniform array that meets half the wavelength, the system requires a large number of transmitting and receiving antenna elements. The number of array elements is huge, and working in the high frequency band may result in mutual coupling between array elements, leading to complex system design, difficult engineering implementation, and high cost[3]. Nowadays, traditional 3D reconstruction algorithms are mostly used in millimeter-wave array imaging, which makes it difficult to achieve real-time high-resolution imaging. Because of this, traditional array imaging faces the contradiction between imaging accuracy, imaging speed, and system cost in practical engineering applications, making it difficult to reconcile.

In millimeter-wave security imaging, to improve the focusing effect of near-field energy, the security system can use a beam pattern with the appropriate SideLobe Level (SLL), main lobe width, and directionality to capture the 3D information of the human body. In recent years, scholars at home and abroad have proposed many analytical methods to solve the problem of antenna array synthesis, including the Duff Chebyshev and Taylor methods for uniformly distributed antenna arrays[4,5], which reduce the peak SLL but increase the main lobe width. In addition, these uniformly distributed and equidistant arrays require a large number of elements, high hardware costs, and high computational complexity to obtain high-resolution images. To solve these problems, sparse array synthesis technology has emerged, which can not only effectively reduce the number of required array elements, but also ensure appropriate beam patterns. The goal of sparse array synthesis technology is to optimize the spatial response performance of antenna arrays based on certain constraints, such as element arrangement, weight range, main lobe width and SLL, to obtain the minimum number of elements required to achieve specific spatial response performance[6]. At present, sparse array synthesis mainly focuses on the far-field aspect. Lemaitre-Auger Pierre used a subsampled distribution to expand the cell spacing, which could only suppress the generation of pseudo-Bessel beams[7]. Li Peng fa proposed a subarray-based focused array antenna to reduce the number of antennas, but its SLL is relatively high[8]. RUDOLPH D L uses a genetic algorithms to synthesize controllable SLL sparse arrays[9]. However, the method of random optimization is time-consuming and has the problem of local convergence. Compressed Sensing (CS) has the advantage of determining the optimal solution and has been widely applied in various research fields, such as biomedical and sparse array synthesis. To obtain the array with the minimum sparsity in sparse array synthesis, prior and likelihood information are introduced. OLIVERI G respectively adopted single-task Bayesian CS (BCS) [10]and multi-task Bayesian Compressed Sensing (BCS)[11], both of which were solved by a Relevance Vector Machine (RVM), effectively solving the problem of sparse array synthesis. Because the excitation of the array is composed of amplitude and phase, it is a complex number. However, single-task BCS can only solve real number excitation problems, whereas multi-task BCS is suitable for solving complex excitation problems. However, both are based on point estimation, and the adaptability of excitation weights is not strong. Therefore, most existing sparse array synthesis techniques focus on the sparsity process of far-field uniform arrays, and face problems such as difficulty in solving, local convergence, and weak weight adaptability. However, there is little research on sparse array imaging processing.

After obtaining echoes through the designed sparse array, high-resolution imaging is performed. Near-field sparse array imaging commonly uses time-domain and frequency-domain imaging algorithms. A typical near-field time-domain imaging algorithm is the Back Projection Algorithm (BPA), which has a simple and easy to implement imaging principle[12] and can be applied to various imaging scenarios. However, time-domain algorithms first need to partition the imaging scene into grids, and then coherently accumulate the imaging for each point to ensure imaging accuracy. The computational complexity is proportional to the number of array elements and the number of pixels in the imaging scene, which results in lower computational efficiency when applied to 3D imaging. Compared with time-domain algorithms, frequency-domain algorithms transform the echo signal into the spatial domain for compensation, avoiding the need to divide the imaging scene into grids, reducing computational complexity, and improving efficiency. A typical near-field frequency-domain imaging algorithm is the Range Migration Algorithm (RMA), which requires interpolation to compensate in the wavenumber domain during the imaging process[13]. However, a finite length interpolation kernel function can introduce truncation errors and reduce imaging accuracy. Therefore, there is a contradiction between imaging accuracy and imaging speed, which makes it difficult to meet the current needs of human security imaging.

Based on the aforementioned analysis, this paper proposes a trustworthy inference near-field sparse synthesis array 3D millimeter-wave imaging algorithm, which models near-field sparse arrays as a pattern matching problem. The error between the synthesized sparse array pattern and the expected target pattern is equivalently transformed into a Bayesian inference problem. BCS is used to determine the array with the minimum sparsity that is close to the target reference pattern. The algorithm first models the complex excitation weights as Laplacian priors. Due to the non-conjugate nature of the prior and likelihood, hierarchical Bayesian modeling is performed based on the prior modeling to construct the relationship between the likelihood function and Laplacian prior parameters, and then, the posterior probability density function of the complex excitation weights is derived. In addition, to ensure the closed analytical solution of the posterior probability density function, the Variational Bayesian Expectation Maximization (VB-EM) method is applied to calculate the posterior probability density functions of the complex array weights and their hyperparameters based on the Gaussian Seidel iteration strategy. Finally, using the results of the posterior probability density function, the analytical optimal value, confidence interval, and confidence level of the complex array weights are obtained, thereby achieving an analytical indication of the dynamic changes in the complex array weights. In terms of image processing, the designed sparse array receives human echo data and performs dimensionality processing. In the height distance dimension, the Fast Factorized Back Projection (FFBP) algorithm is used to decompose the array into multiple sub-apertures. Then, adjacent sub-images are recursively fused through linear interpolation to complete the two-dimensional (2D) reconstruction of the height distance dimension. In the azimuth distance dimension, the BPA is used to complete the 2D reconstruction of the azimuth distance dimension. This paper quantitatively analyzes the proposed method by comparing it with traditional sparse array synthesis methods in the simulation experiments. While keeping the aperture unchanged, the sparsity of the array elements is smaller, and the matching accuracy between the synthesized directional pattern and the target directional pattern is better. The measured data via both one-dimensional (1D) electrical scanning and 2D planar full electrical scanning experiments shows that the sparse array designed in this paper achieves a good balance between imaging accuracy, imaging speed, and system cost, while maintaining the same level of sparsity. The effectiveness and superiority of the method proposed in this paper are verified through simulation comparison and experimental verification. The high accuracy of the sparse array reconstruction designed in this paper is validated by the measured data of 1D electrical scanning and 2D planar full electrical scanning.

2 Electrical Scanning Imaging System and Signal Model

The millimeter-wave electric scanning imaging system adopts a linear array electrical scanning in the height dimension and a circular scanning in the azimuth dimension to form a 2D synthetic aperture, to achieve the multi-angle observation capability. This can reduce the number of image reconstructions and improve the scanning efficiency of the system[14], while also collecting 3D echo data, which is very suitable for close range security imaging. The geometric model of the millimeter-wave circumferential scanning imaging system is shown in Fig. 1. A 3D polar coordinate system is established with the origin $O(R,\theta,Z)$, and the person being tested stands at the center of the cylinder. The antenna array forms a Δh uniform linear array with a spacing of in the Z-direction. The linear array is centered R_0 around the Z-axis, and the antenna rotates around the Z-axis with a radius. After scanning the target at each position, the antenna array moves to the next position to continue scanning until the end. The scanning in two dimensions forms a cylindrical scanning surface. The θ angle between the position of the antenna array and the X-axis is defined as the angle interval between each motion. The $\Delta\theta$ pitch beamwidth of the antenna and the rotation range of the linear array determine the 2D resolution of height and azimuth.

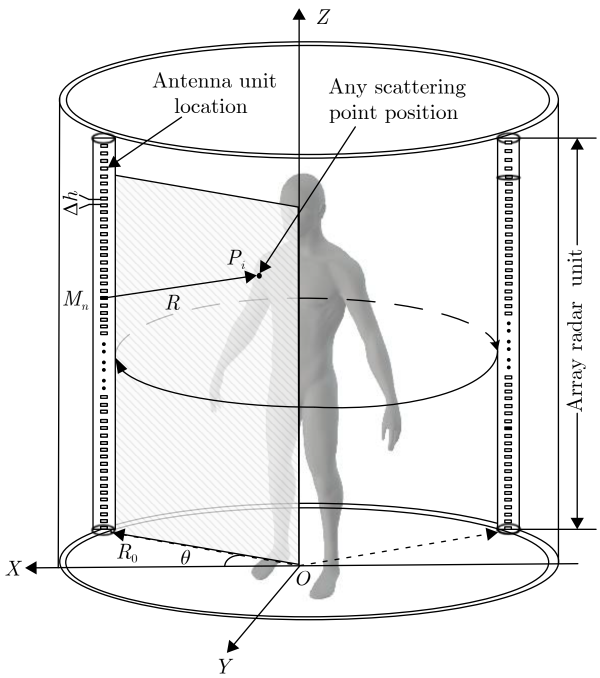

Fig. 1 Geometric model of millimeter-wave electric scanning circumferential 3D imaging system

In the millimeter-wave electrical scanning circular 3D imaging system, to ensure imaging resolution, a large time bandwidth signal is usually used, and the common large time bandwidth signal is a linear frequency modulation signal, whose mathematical expression is expressed as follows:

$$s_{\mathrm{t}}(t) = \mathrm{rect}\left(\frac{t}{T_{\mathrm{p}}}\right)\exp\left\{\mathrm{j}2\pi\left(f_{\mathrm{c}}t+\frac{\gamma}{2}t^2\right)\right\} \tag{1}$$

where t represents fast time, $\mathrm{rect}(\cdot)$ is a rectangular window function, T_{p} represents the time width of the transmitted signal, f_{c} represents the center frequency of the signal (*i.e.*, the carrier frequency), and γ is the frequency modulation slope of the linear frequency modulation signal.

The position of the antenna unit M_n is $(R_0\cos\theta, R_0\sin\theta, z)$. The position of the target scattering point P_i is (x_i, y_i, z_i); then, the distance from the antenna unit M_n to the target scattering point P_i is expressed as follows:

$$R(\theta;z) = \sqrt{(R_0\cos\theta-x_i)^2+(R_0\sin\theta-y_i)^2+(z-z_i)^2} \tag{2}$$

After a delay, the P_i original echo signal M_n received by the antenna unit from the target scattering point is given by the following:

$$s_{\mathrm{r}}(t,\theta,z) = \sigma_i\mathrm{rect}\left(\frac{t-\tau(\theta;z)}{T_{\mathrm{p}}}\right) \cdot\exp\left\{\mathrm{j}2\pi\left[f_{\mathrm{c}}(t-\tau(\theta;z))+\frac{\gamma}{2}(t-\tau(\theta;z))^2\right]\right\} \tag{3}$$

where σ_i is the i backscattering coefficient of the target scattering point, and the echo delay can be expressed as $\tau(\theta;z) = 2R(\theta;z)/\mathrm{c}$,

The echo signal obtained by down converting Eq. (3) is expressed as follows:

$$s(t,\theta,z) = \sigma_i \mathrm{rect}\left(\frac{t-\tau(\theta;z)}{T_\mathrm{p}}\right) \cdot \exp\left\{-\mathrm{j}2\pi f_\mathrm{c}\tau(\theta;z) + \mathrm{j}\pi\gamma(t-\tau(\theta;z))^2\right\} \tag{4}$$

The pulse compression of Eq. (4) is performed through matched filtering, usually selecting the time-domain flipped conjugate signal of the linear frequency modulation part of the transmitted signal as the matched filter for pulse compression, which can be expressed as follows:

$$h(t) = \exp\{-\mathrm{j}\pi\gamma(-t)^2\} \tag{5}$$

The process of pulse compression is usually achieved by multiplying the frequency domain of the signal, which is written as follows:

$$\begin{aligned} s_O(t,\theta,z) &= \mathrm{FFT}^{-1}\{\mathrm{FFT}[s(t,\theta,z)] \cdot \mathrm{FFT}[h(t)]\} \\ &= \sigma_i \,\mathrm{sinc}\left(\frac{t-\tau(\theta;z)}{T_\mathrm{p}}\right) \exp(-\mathrm{j}2\pi f_\mathrm{c}\tau(\theta;z)) \end{aligned} \tag{6}$$

where FFT^{-1} represents the inverse fast Fourier transform. From Eq. (6), it can be seen that, after the pulse compression processing of the matched filtering, the echo signal exhibits a sinc functional form in the distance time domain, indicating that the echo has completed the focusing in the distance dimension, but still needs to be focused in the azimuth and altitude dimensions.

3 Sparse Array Synthesis

BCS is one of the existing techniques for synthesizing the expected radiation pattern with the minimum sparsity of the array, which has significant advantages, such as flexibility and high computational efficiency[15]. However, there is still little research on using Bayesian learning for near-field sparse array synthesis. In the framework of sparse Bayesian learning, this paper models the near-field sparse array synthesis problem as a pattern-matching problem. Because the pattern-matching problem is a Non-deterministic Polynomial (NP) problem with polynomial complexity, it is difficult to solve using deterministic methods. Therefore, the sparse array synthesis problem is further formulated as a BCS model. In Bayesian learning, considering the problem of large array size and a large number of elements in reality, this paper aims to use as few elements as possible to synthesize the expected directional pattern. Therefore, heavy-tailed Laplacian sparse priors are applied to the complex excitation weights, and the priors are hierarchically modeled. Finally, Bayesian inference is used to solve the complete posterior probability density function of the optimal sparse array excitation, and its confidence interval and confidence are obtained.

3.1 Array complex excitation hierarchical Bayesian modeling

This paper considers an equivalent model of a circular cylindrical linear array with N uniformly isotropic elements. Before performing sparse synthesis on the near-field array, because the signal received by the receiving end of the near-field array is a spherical wave radiated toward it by the target, it is necessary to first model the near-field focusing array of the uniform array[16], and then use this model as the basis for sparse array synthesis. This paper focuses on targets at different heights using the same array antenna, which is always distributed on the Z-axis of the height dimension. The aperture length of the array is 1.8 m. When the array antenna rotates to a certain azimuth position, the 3D coordinate system is transformed into a 2D coordinate system, and a near-field array focusing model is established at any azimuth, as shown in Fig. 2. The element at the physical center of the array antenna is taken as the reference element $O(0,0)$, which is denoted as the reference origin of the Cartesian coordinate system (assuming the total number of elements is odd).

This paper uses the Cartesian coordinate system to model the near-field array model; hence, only straight lines parallel to the array can be truncated, which is called the focal line. When the focal line is slightly larger than the array, the array performs better and has higher efficiency within this range[17]. For the application scenario of millimeter-wave security check, the distance

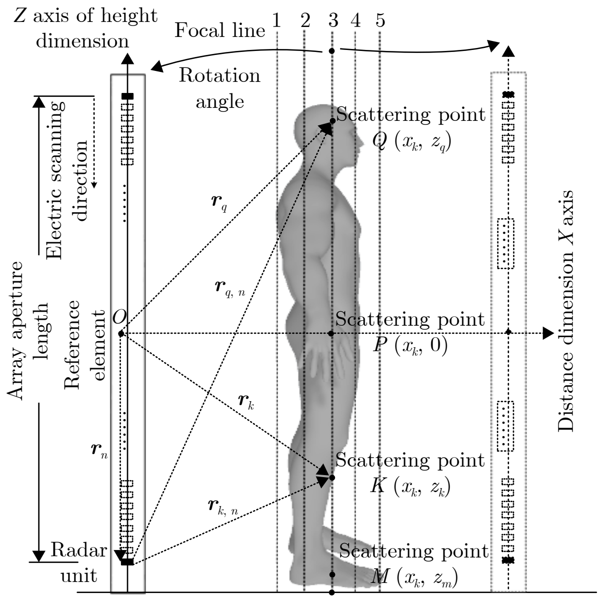

Fig. 2 Focusing model of near-field linear array in a Cartesian coordinate system with arbitrary orientation

between the center of the human body and the height dimension Z-axis is 0.628 m. Therefore, the distance between the focal line and the height dimension Z-axis is set to 0.628 m. As shown in Fig. 2, focal line 3 is selected. To minimize mutual interference and coupling between antennas, the scattering point P at the center of focal line 3 is chosen as the point with the maximum gain, that is, the near-field array modeling is carried out in the orthogonal direction of the antenna array to improve the focusing performance of the antenna array. For any scattering point in space $K(x_k, z_k)$, the vector pointing from the reference point O to the scattering point K is $\boldsymbol{r}_k$, the vector pointing from the reference point O to the $n$element with sequence number is $\boldsymbol{r}_n$, and the $n$vector pointing from the element with sequence number in the array to the scattering point K is $\boldsymbol{r}_{k,n} = \boldsymbol{r}_k - \boldsymbol{r}_n$. Then, the electrical field radiated by the n element with the sequence number at the scattering point K is expressed as follows:

$$\begin{aligned} E_n(\boldsymbol{r}_k) &= f_0(\theta, \psi) w_n \frac{\mathrm{e}^{-\mathrm{j}2\pi|\boldsymbol{r}_{k,\,n}|/\lambda}}{|\boldsymbol{r}_{k,\,n}|} \\ &= f_0(\theta, \psi) w_n \frac{\mathrm{e}^{-\mathrm{j}2\pi|\boldsymbol{r}_k - \boldsymbol{r}_n|/\lambda}}{|\boldsymbol{r}_k - \boldsymbol{r}_n|} \end{aligned} \tag{7}$$

where λ is the working wavelength of the array antenna, $f_0(\theta, \psi)$ represents the element factor of the directional pattern of the array elements. This paper assumes that each element is an ideal omnidirectional antenna (*i.e.*, the element factor $f_0(\theta, \psi) = 1$); w_n is the complex excitation weight corresponding to the numbered element n. By assuming that all elements in a linear array are isotropic, the interference caused by mutual coupling between elements can be ignored, significantly simplifying the analysis and calculation of the array synthesis. The basic principles of a reliable inference sparse array synthesis algorithm are highlighted, and a preliminary design of sparse arrays is proposed. In practical systems, array elements usually have certain directionality and different responses in different directionalities. Omnidirectional array elements are assumed to be unable to capture the impact of the deviation caused by this directionality on imaging. The next step will consider calibrating the phase error caused by array directionality[18]. Therefore, the electrical field radiated by the array antenna of N elements at the scattering point K can be expressed as follows:

$$E(\boldsymbol{r}_k) = \sum_{n=1}^{N} w_n \frac{\mathrm{e}^{-\mathrm{j}2\pi|\boldsymbol{r}_k - \boldsymbol{r}_n|/\lambda}}{|\boldsymbol{r}_k - \boldsymbol{r}_n|} \tag{8}$$

Under near-field millimeter-wave security inspection, the human body being tested is a 3D object. Therefore, $\boldsymbol{r}_k$ in $E(\boldsymbol{r}_k)$ is replaced with the distance vector in the near-field observation area to form the beam pattern in the observation area. Based on the superposition principle, the electrical field radiated by the linear array at the observation point $E(\boldsymbol{r})$ in the near-field area is represented as follows:

$$E(\boldsymbol{r}) = \sum_{n=1}^{N} w_n \frac{\mathrm{e}^{-\mathrm{j}2\pi|\boldsymbol{r} - \boldsymbol{r}_n|/\lambda}}{|\boldsymbol{r} - \boldsymbol{r}_n|} \tag{9}$$

where $\boldsymbol{r}$ is the distance vector from the near-field observation point to the reference point. By discretization, Eq. (9) is rewritten in matrix form as follows:

$$\boldsymbol{E} = \boldsymbol{\Phi} \boldsymbol{w} \tag{10}$$

where $\boldsymbol{E} = [E(\boldsymbol{r}_{O1}), E(\boldsymbol{r}_{O2}), \cdots, E(\boldsymbol{r}_{OK})]^{\mathrm{T}}$ contains the sample vectors at K different observation positions, $\boldsymbol{w} = [w_1, w_2, \cdots, w_N]^{\mathrm{T}}$ is the complex excitation weight vector of N elements, the position of each element in $\boldsymbol{w}$ represents the position of the antenna element, and the size of each element represents the amplitude of the antenna element excitation. Under near-field millimeter-wave security inspection, the directional vector matrix $\boldsymbol{\Phi}$ can be written as follows:

$$\boldsymbol{\Phi}=\left\{\begin{array}{cccc}\dfrac{\exp(-\mathrm{j}2\pi\left|\boldsymbol{r}_{O1}-\boldsymbol{r}_1\right|/\lambda)}{\left|\boldsymbol{r}_{O1}-\boldsymbol{r}_1\right|} & \dfrac{\exp(-\mathrm{j}2\pi\left|\boldsymbol{r}_{O1}-\boldsymbol{r}_2\right|/\lambda)}{\left|\boldsymbol{r}_{O1}-\boldsymbol{r}_2\right|} & \cdots & \dfrac{\exp(-\mathrm{j}2\pi\left|\boldsymbol{r}_{O1}-\boldsymbol{r}_N\right|/\lambda)}{\left|\boldsymbol{r}_{O1}-\boldsymbol{r}_N\right|} \\ \vdots & \ddots & & \vdots \\ \dfrac{\exp(-\mathrm{j}2\pi\left|\boldsymbol{r}_{OK}-\boldsymbol{r}_1\right|/\lambda)}{\left|\boldsymbol{r}_{OK}-\boldsymbol{r}_1\right|} & \dfrac{\exp(-\mathrm{j}2\pi\left|\boldsymbol{r}_{OK}-\boldsymbol{r}_2\right|/\lambda)}{\left|\boldsymbol{r}_{OK}-\boldsymbol{r}_2\right|} & \cdots & \dfrac{\exp(-\mathrm{j}2\pi\left|\boldsymbol{r}_{OK}-\boldsymbol{r}_N\right|/\lambda)}{\left|\boldsymbol{r}_{OK}-\boldsymbol{r}_N\right|}\end{array}\right\} \quad (11)$$

The purpose of sparse array synthesis is to find the array with the least number of elements and the complex excitation weights of the correlated elements, so that its radiation pattern matches the expected reference pattern $\boldsymbol{E}_{\text{ref}}$ with a matching error of $\boldsymbol{e}$. Then, this problem can be transformed into an ℓ_0-norm constrained pattern-matching optimization problem, and the matching model is shown in the following equation:

$$\min\ \|\boldsymbol{w}\|_0\ \text{s.t.}\ \|\boldsymbol{E}_{\text{ref}}-\boldsymbol{\Phi}\boldsymbol{w}\|_2^2<\boldsymbol{e} \quad (12)$$

where $\|\cdot\|_0$ represents the ℓ_0-norm, which constrains the number of non-zero complex excitation weight $\boldsymbol{w}$, and the number of complex excitation weight $\boldsymbol{w}$ is the number of elements in the array. Constraining the number of non-zero complex excitation weights is equivalent to constraining the number of non-zero elements in the array. $\|\cdot\|_2$ represents the ℓ_2-norm, which constrains the matching accuracy between the sparse array synthesized directional pattern and the reference directional pattern, $\boldsymbol{E}_{\text{ref}}=[E_{\text{ref}}(\boldsymbol{r}_{O1}),E_{\text{ref}}(\boldsymbol{r}_{O2}),\cdots,E_{\text{ref}}(\boldsymbol{r}_{OK})]^{\text{H}}\in C^K$ is the sample vector of the near-field reference directional pattern at K different observation positions, and $\boldsymbol{e}=[e(\boldsymbol{r}_{O1}),e(\boldsymbol{r}_{O2}),\cdots,e(\boldsymbol{r}_{OK})]^{\text{H}}\in C^K$ is the zero-mean complex Gaussian error vector with an accuracy of β.

The problem represented by Eq. (12) is an NP-hard problem that is difficult to solve using deterministic methods. Random optimization may be a suitable method to solve this problem, but it faces the problem of local convergence[19] and has poor performance due to complex high-dimensional problems. BCS has been used in far-field sparse array synthesis[10]. To express the near-field sparse array synthesis problem as a BCS problem, the ℓ_2-norm constraint in Eq. (12) is further expressed as follows:

$$\boldsymbol{E}_{\text{ref}}=\boldsymbol{\Phi}\boldsymbol{w}+\boldsymbol{e} \quad (13)$$

In order to find the array with the minimum number of elements and the complex excitation weights of the elements, so that the radiation pattern matches the expected reference pattern, it is difficult to transform Eq. (12), which uses deterministic methods, into Eq. (13), which formulates the problem as a Bayesian compressive sensing approach. Essentially, the problem of minimizing the ℓ_0-norm of the complex excitation weight $\boldsymbol{w}$ in Eq. (12) is transformed into the problem of solving the complete posterior distribution of the complex excitation weight $\boldsymbol{w}$ in Eq. (13).

Assuming that the error $\boldsymbol{e}$ follows a $\boldsymbol{\beta}$ zero-mean symmetric complex Gaussian distribution with an accuracy of, the $\boldsymbol{E}_{\text{ref}}$ likelihood function of the reference pattern can be obtained as follows:

$$\begin{aligned}p(\boldsymbol{E}_{\text{ref}}|\boldsymbol{w},\boldsymbol{\beta})&=\text{CN}(\boldsymbol{E}_{\text{ref}}|\boldsymbol{\Phi}\boldsymbol{w},\boldsymbol{\beta}^{-1}\boldsymbol{I})\\&=\left(\frac{\boldsymbol{\beta}}{\pi}\right)^K\exp\left(-\boldsymbol{\beta}\left\|\boldsymbol{E}_{\text{ref}}-\boldsymbol{\Phi}\boldsymbol{w}\right\|_2^2\right)\end{aligned} \quad (14)$$

Considering the randomness of errors, the error accuracy $\boldsymbol{\beta}$ is modeled as a Gamma distribution, as follows:

$$p(\boldsymbol{\beta}|c,d)=\text{Gamma}(\boldsymbol{\beta}|c,d)=\frac{d^c}{\Gamma(c)}\boldsymbol{\beta}^{c-1}\exp(-d\boldsymbol{\beta}) \quad (15)$$

where $\Gamma(c)=\int_0^\infty t^{c-1}\mathrm{e}^{-t}\mathrm{d}t$ is the Gamma function, d is a constant parameter[20], and c can be taken as 10^{-3} based on empirical values.

Considering that the array size is too large and the cost is too high in reality, this paper applies heavy-tailed Laplacian sparse priors to the complex excitation weight $\boldsymbol{w}$ to synthesize the desired radiation pattern with fewer array elements[21,22]. After obtaining the prior model and likelihood function of the complex excitation weights, the joint posterior distribution of the complex excitation weights can be obtained based on Bayesian principles, and then, the posterior analytical solution of the complex excitation weights can be solved based on Bayesian inference. However, due to the non-conjugate nature of the heavy-tailed Laplacian sparse prior and Gaussian likelihood function, it is not possible to derive a closed-form analytical solution for the posterior probability density function. Therefore, this paper introduces intermediate hyperparameters to perform hierarchical Bayesian modeling on the Laplacian sparse prior model with heavy tails, to achieve the solution of the complete posterior probability density function of complex excitation weights.

In the first step of the hierarchical model, this paper models $\boldsymbol{w}$ as a complex Gaussian distribution that depends on hyperparameter $\boldsymbol{\alpha}$. The modeling is written as follows:

$$p(\boldsymbol{w}\,|\boldsymbol{\alpha}) = \prod_{i=1}^{N} \mathrm{CN}(w_i\,|0,\alpha_i) = \prod_{i=1}^{N} \frac{1}{\pi\alpha_i}\exp\left(-\frac{w_i^2}{\alpha_i}\right) \tag{16}$$

Due to the inherent smoothness of Gaussian functions, Eq. (16) does not belong to the sparse distribution range. To promote the sparsity of priors and simplify the derivation of posterior distributions, this paper selects the gamma distribution conjugate with Gaussian distribution as the prior of hyperparameter $\boldsymbol{\alpha}$ and models the hyperparameter $\boldsymbol{\alpha}$ in the second step of the hierarchical model, as follows:

$$\begin{aligned} p(\boldsymbol{\alpha}\,|a,b) &= \prod_{i=1}^{N}\mathrm{Gamma}(\alpha_i\,|a,b) \\ &= \prod_{i=1}^{N}\frac{b^a}{\Gamma(a)}\alpha_i^{a-1}\exp(-b\alpha_i) \end{aligned} \tag{17}$$

According to Eqs. (16) and (17), the edge distribution of the complex excitation weight $\boldsymbol{w}$ can be calculated, *i.e.*, $p(\boldsymbol{w}) = \int p(\boldsymbol{w}\,|\boldsymbol{\alpha})p(\boldsymbol{\alpha}\,|a,b)\mathrm{d}\boldsymbol{\alpha}$. When the value of a is 1.5, the edge distribution follows a Laplace distribution[20], and b based on empirical values, b can be taken as 10^{-6}. The probability models of parameters and hyperparameters in the hierarchical Bayesian model are shown in Fig. 3. In Fig. 3, $\boldsymbol{E}_{\mathrm{ref}}$ represents the reference direction diagram, $\boldsymbol{w}$ represents the complex excitation weight, and $\boldsymbol{\alpha}$, β represents the introduced hyperparameter random variables. The layering of $\boldsymbol{w}$ and $\boldsymbol{\alpha}$ can simplify the model by making non conjugate problems solvable. The dashed boxes a, b, c, and d are all fixed parameters.

3.2 Array complex excitation variational inference solution

According to the Bayesian hierarchical model given in Section 3.1, the joint posterior probability distribution of the incentive weight $\boldsymbol{w}$ and hyperparameters $\boldsymbol{\alpha}$ and $\boldsymbol{\beta}$ is calculated using Bayesian inference theory, as follows:

$$p(\boldsymbol{w},\boldsymbol{\alpha},\boldsymbol{\beta}\,|\boldsymbol{E}_{\mathrm{ref}}) = \frac{p(\boldsymbol{E}_{\mathrm{ref}}\,|\boldsymbol{w},\boldsymbol{\beta})p(\boldsymbol{w}\,|\boldsymbol{\alpha})p(\boldsymbol{\alpha})p(\boldsymbol{\beta})}{p(\boldsymbol{E}_{\mathrm{ref}})} \tag{18}$$

The numerator in Eq. (18) can be obtained from Eqs. (14) to (17). However, it is necessary to calculate the complete posterior distribution of the complex excitation weight $\boldsymbol{w}$ to optimize the number of elements in the array. However, calculating the denominator term in Eq. (18) requires multidimensional integration, which is difficult to handle. For reasonable accuracy and efficiency, VB-EM is a typical deterministic approximation algorithm that can effectively infer the hidden random variables and obtain the posterior distribution analytical solutions of random variables through the expectation maximization method.

This paper considers $\boldsymbol{w}$, $\boldsymbol{\alpha}$, $\boldsymbol{\beta}$, $\boldsymbol{E}_{\mathrm{ref}}$ as random variables, where $\boldsymbol{E}_{\mathrm{ref}}$ can be measured and is an explicit random variable and $\boldsymbol{w}$, $\boldsymbol{\alpha}$, $\boldsymbol{\beta}$ cannot be directly measured and is an implicit random variable. An implicit random variable is included in the combination of random variables $Z=\{\boldsymbol{w},\ \boldsymbol{\alpha},\ \boldsymbol{\beta}\}$. The posterior probability density functions of these implicit random variables can be obtained by solving VB-EM. The logarithmic

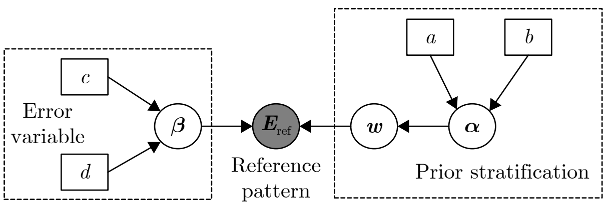

Fig. 3 Bayesian graphic model

likelihood function of Eq. (14) can be expressed as follows:

$$\ln p(\boldsymbol{E}_{\text{ref}}) = \text{ELBO}(q) + \text{KL}(q \,\|p) \tag{19}$$

where

$$\text{ELBO}(q) = \int q(\boldsymbol{Z}) \ln \left(\frac{p(\boldsymbol{E}_{\text{ref}}, \boldsymbol{Z})}{q(\boldsymbol{Z})} \right) \mathrm{d}\boldsymbol{Z} \tag{20}$$

$$\text{KL}(q \,\|p) = -\int q(\boldsymbol{Z}) \ln \left(\frac{p(\boldsymbol{Z} \,|\boldsymbol{E}_{\text{ref}})}{q(\boldsymbol{Z})} \right) \mathrm{d}\boldsymbol{Z} \tag{21}$$

Here, $q(\boldsymbol{Z})$ is the approximate posterior probability density function, $\text{ELBO}(q)$ represents the lowest evidence lower bound, and $\text{KL}(q \,\|p)$ represents the divergence (KL) between the prior probability density function $p(\boldsymbol{Z} \,|\boldsymbol{E}_{\text{ref}})$ and the approximate posterior probability density function $q(\boldsymbol{Z})$. Because $\text{KL}(q \,\|p) \geq 0$, therefore $\ln p(\boldsymbol{E}_{\text{ref}}) \geq \text{ELBO}(q)$, the increase in the logarithmic likelihood function is always greater than the increase in the lower bound, ensuring the convergence of the algorithm with the lowest evidence lower bound.

In the VB-EM algorithm, based on the assumption of mean field theory, we can simplify the derivation by factoring $q(\boldsymbol{Z})$. Thus, $q(\boldsymbol{Z})$ can be approximated as follows:

$$q(\boldsymbol{Z}) \approx q(\boldsymbol{w}) q(\boldsymbol{\alpha}) q(\boldsymbol{\beta}) \tag{22}$$

Based on the factorization of Eq. (22), the VB-EM algorithm maximizes the lower bound $\text{ELBO}(q)$ relative to q. By substituting Eq. (22) into Eq. (20), the corresponding solution for the random variable can be obtained as follows:

$$\hat{q}(\boldsymbol{Z}_i) \approx \exp\{< \ln p(\boldsymbol{E}_{\text{ref}}, \boldsymbol{Z}) >_{q(\boldsymbol{Z})/q(\boldsymbol{Z}_i)}\} + \text{const} \tag{23}$$

where $i = 1$, 2, 3 corresponds to the posterior probability density function number of $\boldsymbol{\alpha}$, $\boldsymbol{w}$, $\boldsymbol{\beta}$, and $< \cdot >_{q(\boldsymbol{Z})/q(\boldsymbol{Z}_i)}$ represents the $\boldsymbol{Z}_i$ expected operator $\boldsymbol{Z}$ with respect to anything other than $\boldsymbol{Z}$. According to Eq. (23), the $\boldsymbol{Z}$ approximate posterior probability density function of each element in $\boldsymbol{Z}$ can be inferred.

The approximate posterior probability density function of the complex excitation weight $\boldsymbol{w}$ is written as follows:

$$\begin{aligned} \hat{q}(\boldsymbol{w}) \approx\ & \exp\{< \ln p(\boldsymbol{E}_{\text{ref}} \,|\boldsymbol{w}, \boldsymbol{\beta}) p(\boldsymbol{w} \,|\boldsymbol{\alpha}) >_{q(\boldsymbol{\alpha})q(\boldsymbol{\beta})} \\ & + \text{const}\} \end{aligned} \tag{24}$$

By substituting Eqs. (14) and (16) into Eq. (24), it can be concluded that the complex excitation weight $\boldsymbol{w}$ follows a complex Gaussian distribution, as follows:

$$\hat{q}(\boldsymbol{w}) \approx \prod_{m=1}^{N} \text{CN}\left(w_m \,|\boldsymbol{\mu}, \boldsymbol{\Sigma}\right) \tag{25}$$

where

$$\boldsymbol{\mu} = < \boldsymbol{\beta} > \boldsymbol{\Sigma} \boldsymbol{\Phi}^{\text{H}} \boldsymbol{E}_{\text{ref}} \tag{26}$$

$$\boldsymbol{\Sigma} = \left(< \boldsymbol{\beta} > \boldsymbol{\Phi}^{\text{H}} \boldsymbol{\Phi} + < \boldsymbol{A} > \right)^{-1} \tag{27}$$

Here, $\boldsymbol{A} = \text{diag}(\alpha_1^{-1}, \alpha_2^{-1}, \cdots, \alpha_N^{-1})$, $(\cdot)^{-1}$ is the inverse operator, H is the conjugate transpose operator, and the mean of Eq. (26) can be understood as the optimal value of the sparse complex excitation weight $\boldsymbol{w}$. When the value of the complex excitation weight is less than 0.03 times the maximum value, the complex excitation weight is set to zero, and there are no elements at that position. Eq. (27) is the covariance matrix. Based on the set significance level, the upper and lower confidence limits of the optimal value can be calculated, thereby determining the confidence interval and confidence level of the optimal value.

Similarly, according to Eq. (23), the approximate posterior probability density function of hyperparameter $\boldsymbol{\alpha}$ can be obtained as follows:

$$\hat{q}(\boldsymbol{\alpha}) \approx \exp\{< \ln p(\boldsymbol{w} \,|\boldsymbol{\alpha}) p(\boldsymbol{\alpha}) >_{q(\boldsymbol{w})} + \text{const}\} \tag{28}$$

Substituting Eqs. (16) and (17) into Eq. (28), each $\boldsymbol{\alpha}$ element obtained follows a generalized inverse Gaussian distribution with an l-order distance of

$$< \alpha_i^l > = \left(\frac{< 2|w_i|^2 >}{2b} \right)^{\frac{l}{2}} \frac{\mathcal{K}_{\eta-1+l}\left(\sqrt{2b < 2|w_i|^2 >} \right)}{\mathcal{K}_{\eta-1}\left(\sqrt{2b < 2|w_i|^2 >} \right)} \tag{29}$$

where $\mathcal{K}_a$ is the second type of modified Bessel function[20]. When $l = -1$, the updated $< \alpha_i^{-1} >$ is used for Eq. (27).

Similarly, according to Eq. (23), the approximate posterior probability density function of hyperparameter $\boldsymbol{\beta}$ can be obtained as follows:

$$\hat{q}(\boldsymbol{\beta}) \approx \exp\{< \ln p(\boldsymbol{E}_{\text{ref}} \,|\boldsymbol{w}, \boldsymbol{\beta}) p(\boldsymbol{\beta}) >_{q(\boldsymbol{w})q(\boldsymbol{\beta})} + \text{const}\} \tag{30}$$

Substituting EqS. (14) and (15) into Eq. (30), $\boldsymbol{\beta}$ follows a gamma distribution, and the mean value of $\boldsymbol{\beta}$ is written as follows:

$$<\boldsymbol{\beta}>=\frac{K+c}{\|\boldsymbol{E}_{\text{ref}}-\boldsymbol{\Phi}\boldsymbol{w}\|_2^2+d} \tag{31}$$

According to the mentioned Bayesian inference earlier, we can iteratively update Eqs. (26), (27), (29), and (31) to obtain the complex excitation weight $\boldsymbol{w}$ when the difference between the two iterations does not exceed 10^{-3}. Then, based on the number and position of non-zero elements in the complex excitation weight $\boldsymbol{w}$, we can determine the number and position of elements in the optimized sparse array. In summary, the near-field sparse array synthesis algorithm first sets the initial number of iterations, the total number of iterations, the convergence judgment threshold, and the initial values of the iteration variables. Then, the algorithm continuously iterates and updates until the convergence threshold is met, obtaining the optimal value, confidence interval, and confidence level of the complex excitation weight, and achieving a reliable inference of the complex excitation weight. When the sparse array synthesis algorithm reaches the maximum number of iterations, the output may not be the optimal solution of the complex excitation weight, but it can serve as a starting point for subsequent optimization or further processing. Based on this output, the quality and convergence speed of the solution can be improved by adjusting the algorithm parameters and increasing the number of iterations. The flowchart of the sparse array synthesis algorithm is shown in Fig. 4.

4 Improved 3D Time-Domain Imaging Algorithm Based on Sparse Array

After using the near-field sparse array designed in Section 3 to receive the measured echo data of the human body obtained from cylindrical scanning, due to the sparse synthesis of the uniform array, the distribution of excitation weights in the array is asymmetric, *i.e.*, some elements have larger weights, and others have smaller weights. This will cause the sidelobes of the point spread function of the target scattering points to increase, resulting in defocusing and artifacts in the image. By improving the 3D time-domain imaging algorithm based on the sparse array, the sparse recovery of range pulse compressed echo data is achieved to obtain the near-

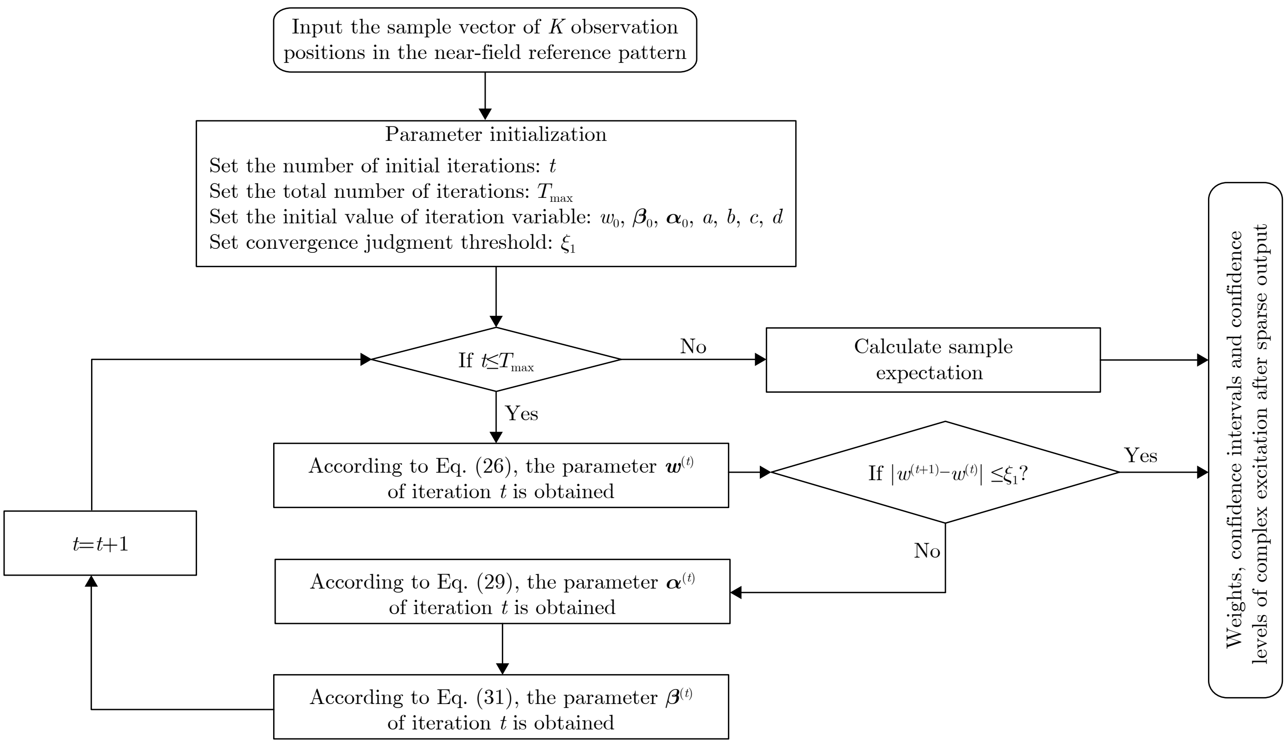

Fig. 4 Flow chart of near-field sparse array synthesis algorithm

field sparse array 3D recovery imaging of the human body. First, the FFBP algorithm is used to focus the image on the height distance dimension. This algorithm mainly uses aperture decomposition and recursive fusion for imaging, and its processing procedure is as follows[23].

To facilitate the sparse synthesis processing of millimeter-wave Multi-Input Multi-Output (MIMO) arrays, the signal model of millimeter-wave MIMO radar is simplified based on the equivalent phase center approximation. The multi-transmitter multi-receiver array structure is transformed into a uniform array with transmitter and receiver co-located, which is equivalent to a phase center with transmitter and receiver co-located at their center positions. The FFBP algorithm divides the entire equivalent phase center aperture into several shorter sub- apertures, according to a certain decomposition coefficient, and projects the compressed data corresponding to the sub-apertures onto a local polar coordinate grid with the aperture center as the origin, thereby obtaining coarse angular domain resolved sub-images. Because the quality of sub-images in the initial stage directly affects the accuracy of subsequent image fusion, it is necessary to introduce the judgment of the integrated aperture in the sub-aperture Back Projection (BP) integration process in the initial stage. Assuming the total length of the linear array aperture is L_{all}, the number of sub apertures in the $n(n=1,2,\cdots,N)$ stage is $U^{(n)}=U^{(1)}/2^{n-1}$, the length of each sub aperture is $l^{(n)}{=}L_{\mathrm{all}}/U^{(n)}$, and $\boldsymbol{w}=[w_1,w_2,\cdots,w_N]^{\mathrm{T}}$ is the complex excitation weight vector of N elements. Each $\boldsymbol{w}$ element in the vector is composed of amplitude and phase, where the position of each element represents the position of the antenna element, and the size of each element represents the amplitude of the antenna element excitation. The height coordinate of the center of sub-aperture $u(u=1,2,\cdots,U^{(n)})$ is $x_u^{(n)}{=}(u-U^{(n)}/2-1/2)\,l^{(n)}$, and the number of elements m contained in each sub aperture depends on the number of sparse complex excitation weight vector $\boldsymbol{w}$ in the current sub-aperture. Each sub aperture image is reconstructed in its own polar coordinate system. In this paper, $\theta_u^{(n)}$ represents the angular domain division of the local polar coordinate system under stage n and sub-aperture u. The local polar coordinate grid of sub-aperture u in the first stage is shown in Fig. 5.

As shown in Fig. 5, for sub-aperture u, a polar coordinate system $(\rho,\theta_u^{(1)})$ is established as the origin $x_u^{(1)}$, where the polar coordinates of the grid pixel point P are $(\rho,\theta_u^{(1)})$, and the elevation beam width of the array element is θ_{beam}. When the angle φ between the direction of the line connecting the array element to the grid pixel point P and the line of sight direction does not exceed $\theta_{\mathrm{beam}}/2$, the array element beam can illuminate the point P, such that

$$-\frac{\theta_{\mathrm{beam}}}{2}\le \arcsin\left[\frac{\left|\xi-\rho\sin\left(\theta_u^{(1)}\right)\right|}{R\left(\rho,\theta_u^{(1)};\xi\right)}\right]\le\frac{\theta_{\mathrm{beam}}}{2},\quad \xi\in\left[-\frac{l^{(1)}}{2},\frac{l^{(1)}}{2}\right] \tag{32}$$

This paper defines ξ, which satisfies Eq. (32) as the integral aperture of the pixel point P. ξ is represented by a symbol ξ^{IA}. For sub-aperture u, as shown in Fig. 5, the echo data from the scattering point P_0 can be written as follows:

$$S(t,\xi)=\sigma_i\,\mathrm{sinc}\left(\frac{t-\dfrac{2R_0}{\mathrm{c}}}{T_{\mathrm{p}}}\right)\exp\left(-\mathrm{j}2\pi f_{\mathrm{c}}\frac{2R_0}{\mathrm{c}}\right) \tag{33}$$

where R_0 is the distance from the aperture position ξ to the target point P_0. When the integral aperture of each pixel on the imaging grid is clearly known, the reconstructed image of the sub-aperture $u$in the first stage is represented as follows:

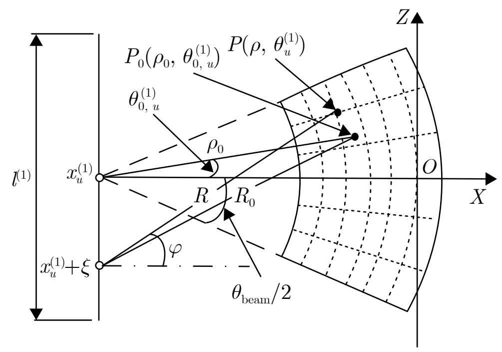

Fig. 5 The first stage of the$u$subaperture of the local polar grid

$$I_u^{(1)}\left(\rho,\theta_u^{(1)}\right)=\int_{\xi\in\xi^{1A}} S(t,\xi)\exp\left(\mathrm{j}K_{Rc}R(\rho,\theta_u^{(1)};\xi)\right)\mathrm{d}\xi \tag{34}$$

where $K_{Rc}=4\pi f_c/c$ is the center frequency wavenumber, and $R(\rho,\theta_u^{(1)};\xi)$ is the distance from the aperture position ξ to the grid pixel point $P(\rho,\theta_u^{(1)})$.

By integrating each sub-aperture separately using Eq. (34), the height distance 2D focused image of the first stage sub-aperture can be obtained, which is a coarse angular domain sub-image.

Second, the previous stage's sub-images are continuously fused with the current stage's sub-images. As recursive fusion continues, the length of the sub-aperture increases while the number of sub-apertures decreases, resulting in an increase in the resolution of the sub-images. The expression for recursive fusion of sub-aperture images is written as follows:

$$\begin{aligned}I_u^{(n)}\left(\rho,\theta_u^{(n)}\right)=\coprod\Big[&I_{2u-1}^{(n-1)}\left(\rho,\theta_{2u-1}^{(n-1)}\right)\\&+I_{2u}^{(n-1)}\left(\rho,\theta_{2u}^{(n-1)}\right)\Big],\end{aligned}$$
$$\begin{cases} n=2,3,\cdots,N\\ u=1,2,\cdots,U^{(n)}\end{cases} \tag{35}$$

where $\coprod$ represents coherent addition. After completing the final stage, the sub aperture is equal to the entire aperture, and the local polar coordinates at this point are equivalent to the global polar coordinate system.

Finally, $I(\rho,\theta)$ is transformed from the polar coordinate image into a Cartesian coordinate system to obtain a resolution image $I(x,z)$ of the entire space.

After the aforementioned FFBP processing, the height distance dimension achieved focusing, while the scattered points in the azimuth dimension still cannot be distinguished. Due to the strong trajectory adaptability of the BP imaging algorithm, it can focus on targets in any nonlinear trajectory. Therefore, the BP algorithm is used for focusing different point targets in the azimuth distance dimension. First, the 3D scene needs to be divided along the height direction into N, a form of overlapping azimuth distance horizontal sections. Then, grid points are divided for each section, and finally, the BP algorithm is used to perform 2D imaging on each horizontal section to obtain a 3D image.

For any 2D horizontal plane XOY, as shown in Fig. 6, we first interpolate a set of distances to the compressed data at each azimuth moment. Then, we calculate the distance R_{ij} between the array element and each point target q on the grid within the rotation range. Based on R_{ij}, we find the corresponding value of the point with coordinates (x_i, y_j) in the 2D data; after phase compensation, the values are coherently accumulated to obtain the reconstruction result of that point, as follows:

$$I(x,y)=\int s_0(t,\theta)\exp(\mathrm{j}K_{Rc}R_{ij})\mathrm{d}y \tag{36}$$

where R_{ij} represents the distance from the array element to the grid point, and $s_0(t,\theta)$ represents the compressed data of the distance-azimuth dimension.

The aforementioned calculation has completed the processing of one section. Repeat the above steps for horizontal sections XOY of different heights until all sections in the direction Z are imaged in two dimensions. Combine the imaging results of the height-distance dimension and the azimuth-distance dimension to obtain the final 3D imaging result of the target, as follows:

$$I(x,y,z)=\{I(x,z),I(x,y)\} \tag{37}$$

Finally, to facilitate the observation and detection of scene targets, the reconstructed 3D human body image is projected along the distance dimension at different observation angles to obtain 2D human body images observed from different angles.

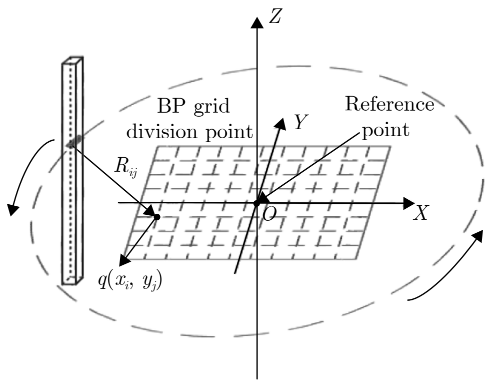

Fig. 6 Two-dimensional horizontal section grid diagram

5 Experimental Verification

To verify the effectiveness and superiority of the proposed credible inference near-field sparse synthesis array for 3D millimeter-wave imaging, simulation experiments were designed. Compared with the ℓ_1-norm[24] based on convex optimization CVX and the synthetic sparse array directional map based on the Focal Undetermined System Solver (FOCUSS)[25] of traditional methods, the credible inference near-field sparse synthesis array provided confidence intervals and confidence levels for complex excitation weight $\boldsymbol{w}$, and the effectiveness and superiority in sparsity and matching performance were verified. Finally, under the same sparsity conditions, the proposed method was validated by collecting 1D electrical scanning circumferential and 2D planar full electrical scanning measured echo data based on the designed sparse array, ensuring imaging results while reducing system complexity.

This section first defines sparsity $\delta = M/M_{\mathrm{UNI}}$, where $M$is the number of non-zero excitation weights $\boldsymbol{w}$ and M_{UNI} is the number of arrays uniformly arranged in the reference pattern. The normalized mean square error ε between the reference pattern and the synthesized pattern is defined as follows:

$$\varepsilon = \frac{\displaystyle\int |\boldsymbol{E}_{\mathrm{ref}}(\boldsymbol{r}) - \boldsymbol{E}(\boldsymbol{r})|^2 \mathrm{d}\boldsymbol{r}}{\displaystyle\int |\boldsymbol{E}_{\mathrm{ref}}(\boldsymbol{r})|^2 \mathrm{d}\boldsymbol{r}} \tag{38}$$

where $\boldsymbol{E}(\boldsymbol{r}) = \boldsymbol{\Phi}\boldsymbol{w}_{\boldsymbol{p}} \in C^K$ is the directional diagram of the final sparse array synthesis. Eq. (38) clearly shows that the mean square error and sparsity of the synthesized directional pattern and the reference directional pattern are inversely proportional. Our goal is to balance the mean square error and sparsity, *i.e.*, to minimize the number of elements in the array, while meeting the desired directional pattern performance as much as possible. Then, sparse array synthesis was carried out based on the convex optimization CVX ℓ_1-norm and the FOCUSS method, respectively. To achieve the same expected directional pattern performance, the sparsity and mean square error were compared. Finally, the designed sparse array was used to receive the echo of the human body, and an improved 3D time-domain imaging algorithm was used to reconstruct the human body in 3D[26], thus verifying the advantage of the proposed algorithm in reducing system complexity while ensuring imaging results.

5.1 Simulation experiment

This section mainly considers a reference pattern with low sidelobes in the near-field. The size of the near-field antenna array used to generate this reference pattern is 191 λ, and a uniform linear array topology with a unit spacing of 0.5 λ is adopted. The total number of array elements is 383, and the position of the near-field focal line from the array is set to 0.628 m, where λ is 0.01035 m. It uses a Taylor distribution reference pattern with a peak SLL of –16 dB. The reference point selects the physical center of the array and uses it as the origin $O(0,0)$ of the coordinates.

The red circles and dashed lines in Fig. 7 represent the reference directional diagram, whereas the blue asterisks and dotted lines represent the algorithm proposed in this paper. The ℓ_1-norm is solved under the convex optimization CVX. The sparse array directional diagram is synthesized under the FOCUSS method. Fig. 7 intuitively shows that the method proposed in this paper is closer to the reference directional diagram and has better matching performance. The red circles and dashed lines in Fig. 8 represent the positions and amplitudes of the reference directional pattern elements, whereas the blue asterisks and dotted lines represent the algorithm proposed in this paper. Based on the ℓ_1-norm solved by convex optimization CVX and the positions and amplitudes of the sparse array directional pattern elements synthesized by the FOCUSS method, Fig. 8 shows that compared with traditional sparse array synthesis methods, the sparsity of the proposed method is lower, and there are more sparse elements in a uniformly arranged full array. To compare the focusing effect of different focal lines, for the application scenario of millimeter-wave security imaging, the distance between the human target and the array is about 0.4～0.8 m. Therefore, the near-field focal lines

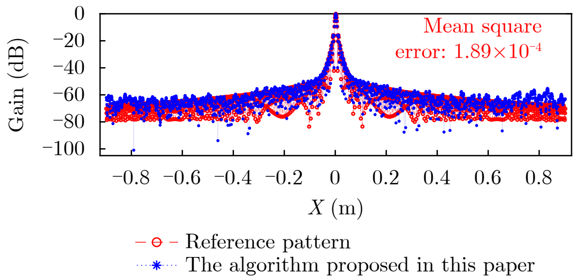

(a) The pattern and reference pattern synthesized by the proposed algorithm

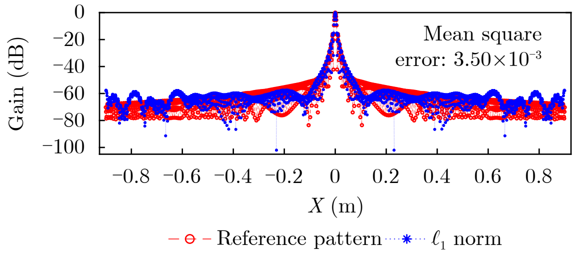

(b) The pattern and reference pattern synthesized by the ℓ_1 norm solved by convex optimization CVX

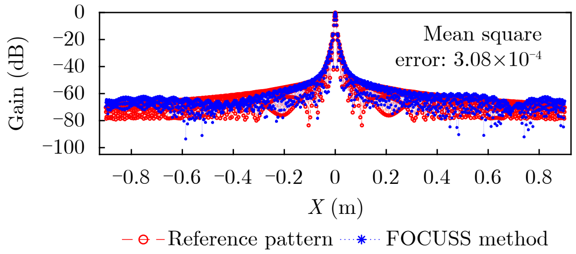

(c) The pattern and reference pattern synthesized by FOCUSS method

Fig. 7 The direction pattern of near-field antenna and the position and amplitude of near-field array under different algorithms

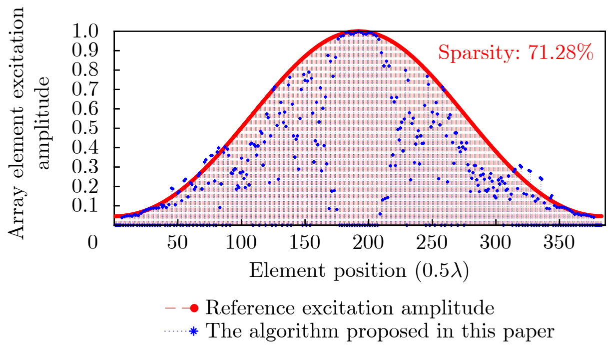

(a) The proposed algorithm synthesizes element positions and amplitudes of the pattern and reference pattern

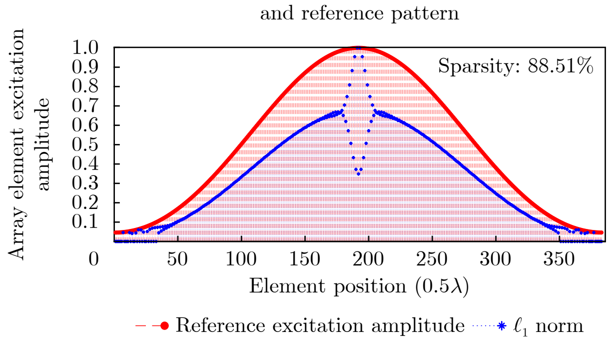

(b) The ℓ_1 norm synthesizes element positions and amplitudes of the pattern and reference pattern based on convex optimization CVX solution

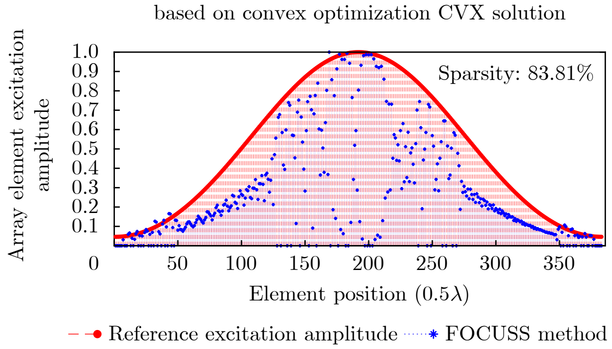

(c) The synthesizes element positions and amplitudes of the pattern and reference pattern based on FOCUSS method

Fig. 8 The position and amplitude of near-field array under different algorithms

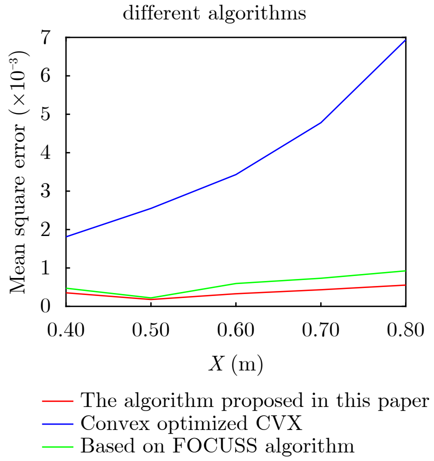

Fig. 9 Different algorithms match the mean square error comparison graph of reference direction graph under different aggregation line positions

are set to 0.4, 0.5, 0.6, 0.7, and 0.8 m. The mean square error of the matching reference direction map at different focal line positions is shown in Fig. 9. It can be seen that the sparse array comprehensive algorithm proposed in this paper has the smallest mean square error in matching the reference direction map.

From the data in Tab. 1, it can be quantitatively observed that, when the performance of the reference directional pattern is almost the same, it can be clearly seen that the algorithm proposed in this paper can make 110 elements sparse with a sparsity of 71.28% compared to other sparse array synthesis algorithms. The normalized mean square error of the sparse array synthesized directional pattern and the reference directional pattern is 1.89×10^{-4}, whereas the ℓ_1-norm sparse array synthesis algorithm based on convex optimization CVX solution makes 44 elements sparse with a sparsity of 88.51% and a mean square error of 3.50 × 10^{-3}. The sparse array synthesis algorithm based on the FOCUSS method makes 62 elements sparse with a sparsity of 83.81% and a mean square error of 3.08 × 10^{-4}. Quantitative analysis shows that the algorithm proposed in this paper has better accuracy in matching reference directional patterns, as well as lower sparsity, and can be designed with lower array costs and system feeding network complexity.

In the framework of sparse Bayesian learning, the algorithm proposed in this paper is used to obtain the posterior probability density function for the analysis of complex excitation weights, thereby obtaining high-order statistical information and obtaining the expected and variance of complex excitation weights. In the case where the mean square error between the direction map synthesized by sparse array and the reference direction map is 1.89 ×10^{-4}, according to the set significance level of 0.05, it can be determined that the maximum amplitude of each element will not exceed the upper limit of the confidence interval, and the minimum amplitude will not be lower than the lower limit of the confidence interval, which can meet the matching performance of the direction map and provide boundary judgment basis for the evaluation of excitation amplitude in practical applications. However, if the lower bound of the confidence interval is directly set to zero, although it improves sparsity, the matching accuracy will be severely reduced. Fig. 10 shows the confidence interval diagram of the positions of near-field array elements and their excitation weight amplitudes, where blue represents the excitation weight amplitude (*i.e.*, expectation) and red represents the confidence interval of the excitation weight at a confidence level of 95%.

5.2 Validation of sparse array reconstructed image with actual test data

To verify the feasibility and applicability of the sparse array synthesized in Section 5.1, as well as the high-precision advantages of the proposed algorithm, this section uses a combination of mechanical and electrical scanning to conduct experimental verification using circumferential measurement data and 2D full electrical scanning array measurement data. The circular imaging system combining mechanical and electrical scanning adopts a linear array that moves along the circumference at a fixed angular velocity, and it performs cylindrical scanning around the measured human body to receive the echo of the human body. The relevant parameters of the millimeter-wave electrical scanning circular imaging system are shown in Tab. 2. The 2D full electrical scanning array imaging system adopts a 2D

Tab. 1 Performance comparison of different sparse array synthesis algorithms

Method	Peak sidelobe level (dB)	Number of array elements	Sparsity (%)	Mean squared error
The method proposed in this article	**–15.81**	**273**	**71.28**	**1.89×10^{-4}**
ℓ_1 norm	–15.76	339	88.51	3.50×10^{-3}
FOCUS method	–15.68	321	83.81	3.08×10^{-4}

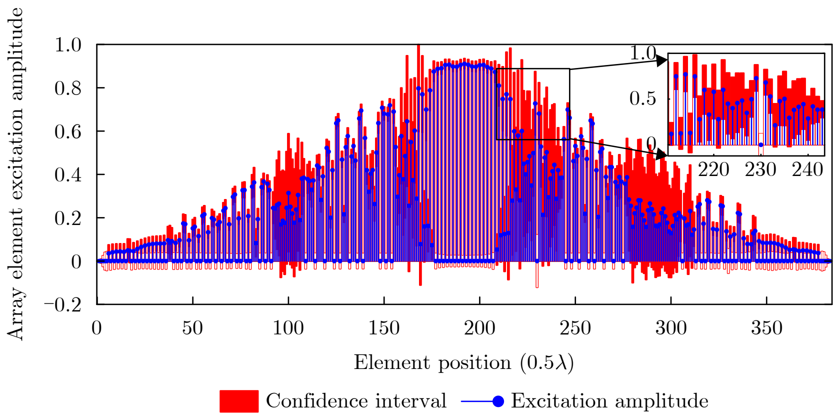

Fig. 10 Confidence interval for the position and amplitude of near-field elements

planar array of 480 × 480 elements, with an antenna array size of 1.0 m × 1.8 m, a spacing of 12.6 mm between elements, a distance of 0.85 m from the center point of the planar array, a system operating frequency of 27 GHz, and a system operating bandwidth of 6.5 GHz. It quickly captures and receives human body echoes from actual measurements.

To qualitatively compare the imaging performance of the sparse array synthesis, based on the sparsity of the algorithm proposed in this paper, the optimal complex excitation weight obtained from the ℓ_1-norm solved by convex optimization CVX is zeroed to a threshold of less than or equal to a certain value, such that the sparsity optimization eliminates the same number of array elements as the algorithm proposed in this paper. Similarly, the optimal complex excitation weight obtained based on the FOCUSS method is zeroed to a threshold of less than or equal to a certain value, such that the sparse optimization reduces the same number of elements as the algorithm proposed in this paper, resulting in the same sparsity of 71.28%. The imaging results shown in Fig. 11(a) are the images obtained by scanning and collecting echo data through a circular linear array, completing 3D imaging processing, and projecting along the maximum distance dimension. Figs. 11(b), 11(c), and 11(d) respectively shows the imaging results of the sparse array designed by the algorithm proposed in this paper, the sparse array designed based on the ℓ_1-norm solved by convex optimization CVX, and the sparse array designed based on the FOCUSS method. The echoes of the human body are collected using the designed sparse array, the 3D reconstruction is completed through an improved 3D time-domain imaging algorithm, and the images are projected along the maximum distance dimension under the same sparsity of 71.28%. The imaging results shown in Fig. 12(a) are obtained by collecting echo data through a 2D full electrical scanning array, completing 3D imaging processing, and projecting along the maximum distance dimension. Figs. 12(b)–(d) respectively shows the imaging results of the sparse array designed by the algorithm proposed in this paper,

Tab. 2 Parameters of millimeter-wave electrical scanning circumferential imaging system

Parameter	Numerical value
System operating bandwidth	6.5 GHz
Operating frequency	27 GHz
Target distance	0.4～0.8 m
Azimuth/elevation angle	55°/55°
Sampling points	64
Element spacing	0.0052 m
Rotation times	314
Single rotation angle	0.2867°
Rotation radius	0.628 m

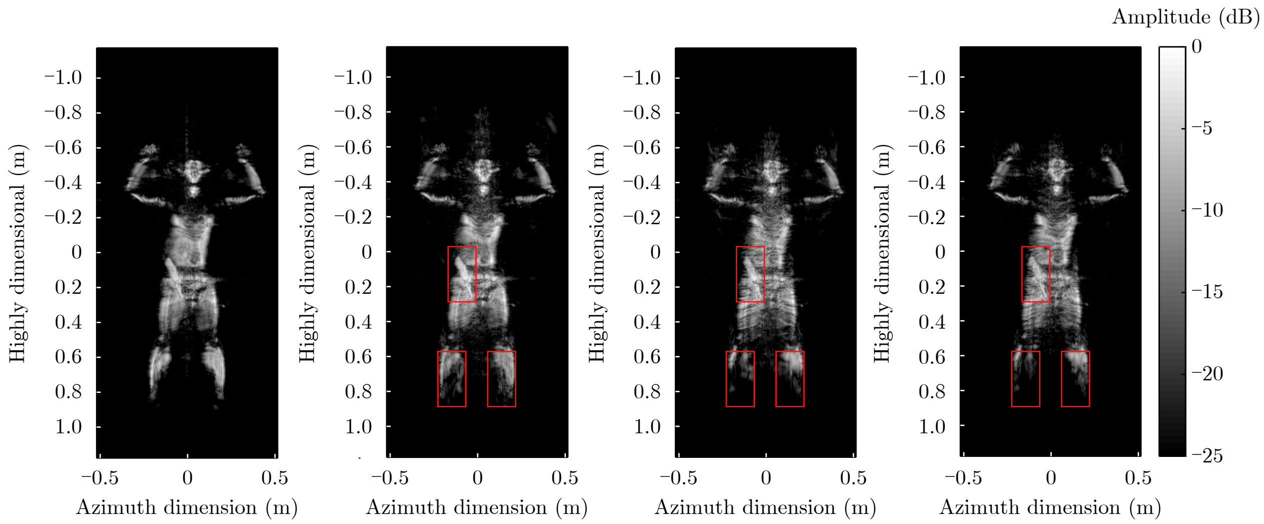

(a) Uniform array imaging

(b) Sparse array imaging results designed by the algorithm proposed in this paper

(c) Sparse array imaging results designed based on the ℓ_1 norm solved by CVX

(d) Sparse array imaging results designed by FOCUSS method

Fig. 11 Comparison of imaging results obtained by circular linear sparse arrays designed by different methods under the same sparsity the sparse array designed based on the ℓ_1-norm solved by convex optimization CVX, and the sparse array designed based on the FOCUSS method. The echoes of the human body are collected using the designed sparse array, the 3D reconstruction is completed through an improved 3D time-domain imaging algorithm, and the images are projected along the maximum distance dimension under the same sparsity of 64.67%. To compare the imaging effects, in all directions, the side imaging results of circular linear sparse arrays designed by different methods at an azimuth of 15° under the same sparsity of 71.28% are shown in Fig. 13. Figs. 13(a)–(d) respectively shows the imaging results of uniform arrays, the sparse array imaging results designed by the algorithm proposed in this paper, the sparse array imaging results designed based on the ℓ_1-norm solved by convex optimization CVX, and the sparse array imaging results designed based on the FOCUSS

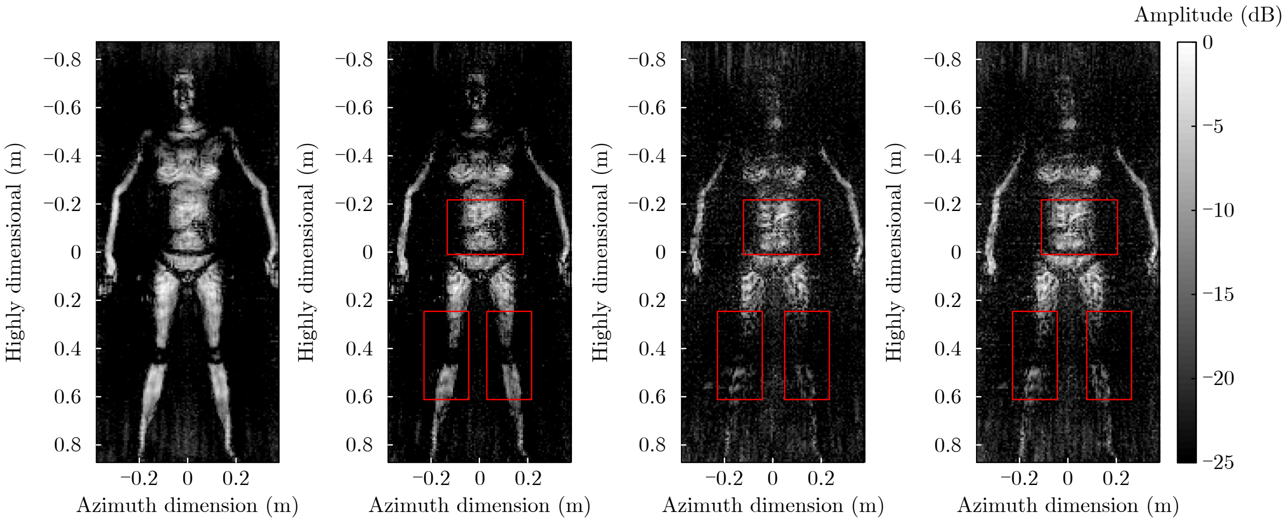

(a) Uniform planar array imaging

(b) Sparse array imaging results designed by the algorithm proposed in this paper

(c) Sparse array imaging results designed based on the ℓ_1 norm solved by CVX

(d) Sparse array imaging results designed by FOCUSS method

Fig. 12 Comparison of imaging results obtained by full scanned planar sparse arrays designed by different methods under the same sparsity

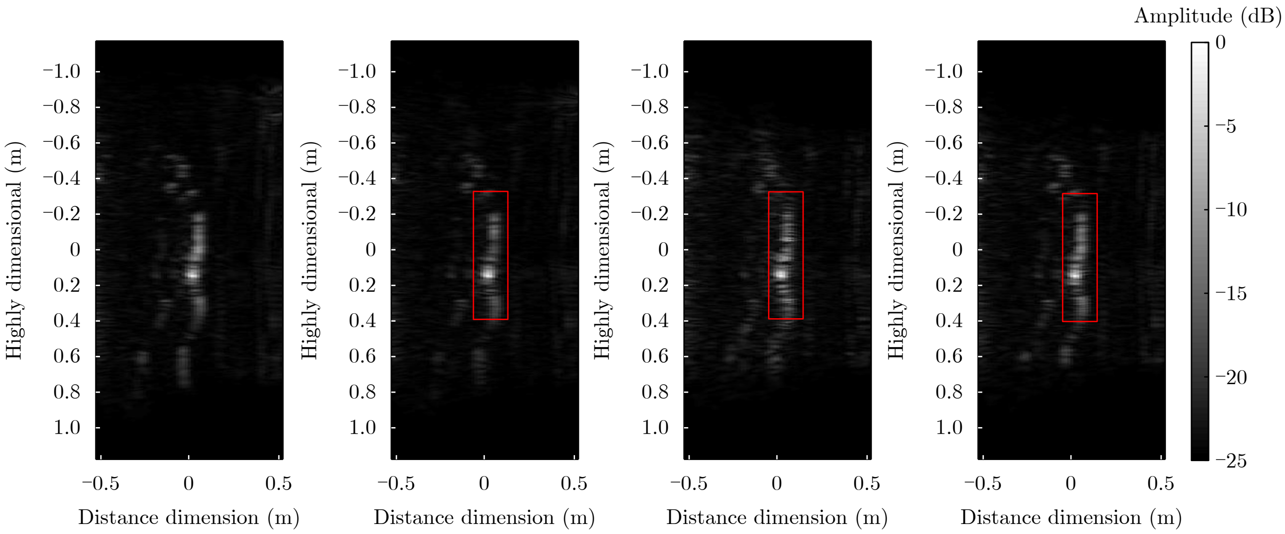

(a) Uniform array imaging

(b) Sparse array imaging results designed by the algorithm proposed in this paper

(c) Sparse array imaging results designed based on the ℓ_1 norm solved by CVX

(d) Sparse array imaging results designed by FOCUSS method

Fig. 13 Comparison of side imaging results of circular linear sparse array designed by different methods at 15° orientation method at an azimuth of 15°.The results show that the focusing effect of the red box example area in Fig. 13(b) is relatively good compared to Figs. 13(c) and (d).

From a qualitative perspective, comparing the results of Figs. 11(b)–(d), and Figs. 12(b)–(d) under the same sparsity, it can be found that Figs. 11(c), (d), and 12(c), 12(d) have poor imaging contrast in the positions where dangerous goods are easily hidden in the human body, such as the left and right thighs and calves, the front waist, the arms, and the chest. The imaging features are severely lost, which affects the detection of dangerous goods and makes it difficult for the security inspection system to be applied in practical situations. Compared with Figs. 11(c) and (d), Fig. 11(b) shows clear imaging of the main locations where dangerous goods are hidden in the human body, with distinct joints and good focusing effect. However, the imaging data volume of Fig. 11(a) is 64 × 383 × 314, whereas the imaging data volume of Fig. 11(b) is 64 × 273 × 314. The imaging data volume of Fig. 12(a) is 64 × 480 × 480, whereas the imaging data volume of Fig. 12(b) is 64 × 386 × 386. Compared with Figs. 11 and 12(a), the results of Figs. 11 and 12(b) show that using the method proposed in this paper for sparse array imaging can reduce the imaging data volume by 28.72% and 35.33%, respectively, while ensuring the imaging quality. The computational complexity of the FFBP algorithm is $O(N^2\log_2 N)$, and the computational complexity of the BP algorithm is $O(N^3)$. Therefore, the high sparsity reliable inference of near-field sparsity proposed in this paper is feasible. The comprehensive array 3D imaging algorithm can reduce the complexity of the system feeding network, while ensuring imaging quality close to the uniform array reference imaging result.

From a quantitative perspective, we conducted point target simulation experiments, as shown in Fig. 14. We selected a 3×3×3 scattering point set, with each point having an isotropic distance of 0.2 m, to form a 27-point simulated cubic model with a size of 0.4 m × 0.4 m × 0.4 m and constant reflection coefficients. We selected an edge point target A from the cubic model and analyzed its focusing performance. We used a uniform array, a sparse array based on the algorithm proposed in this paper, a sparse array based on the FOCUSS algorithm, and an ℓ_1-norm sparse array based on convex optimization CVX to image it. We provided azimuthal and height profile images and quantitatively analyzed their imaging focusing performance. The experimental results are shown in Fig. 15. From Fig. 15 and Tab. 3, it can be seen that, in the azimuth direction, due to the lack of sparse synthesis processing, the imaging profiles of the uniform array, the sparse array algorithm proposed in this paper, the sparse array based on the FOCUSS algorithm, and the ℓ_1-norm sparse array solved by convex optimization CVX have the same peak sidelobe ratio and resolution, and the same imaging quality. In the height direction, it can be seen that the peak sidelobe level of the norm sparse array solved by the sparse array algorithm proposed in this paper is lower, and the resolution is higher compared to the sparse array algorithm proposed in FOCUSS and the ℓ_1-norm sparse array solved by convex optimization CVX. However, compared to that of the uniform array, the peak SLL of the sparse array increased from −24.69 dB to −22.15 dB, *i.e.*, an increase of 2.54 dB, and the imaging quality decreased. However, in the case of significantly reduced array cost and feeding network complexity, the slight decrease in imaging quality due to height is within an acceptable range.

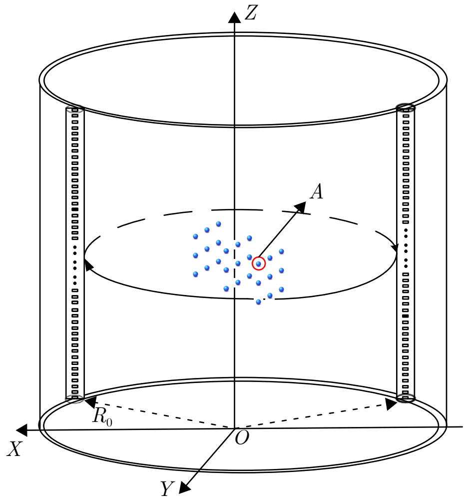

Fig. 14 Diagram of the position of edge point A

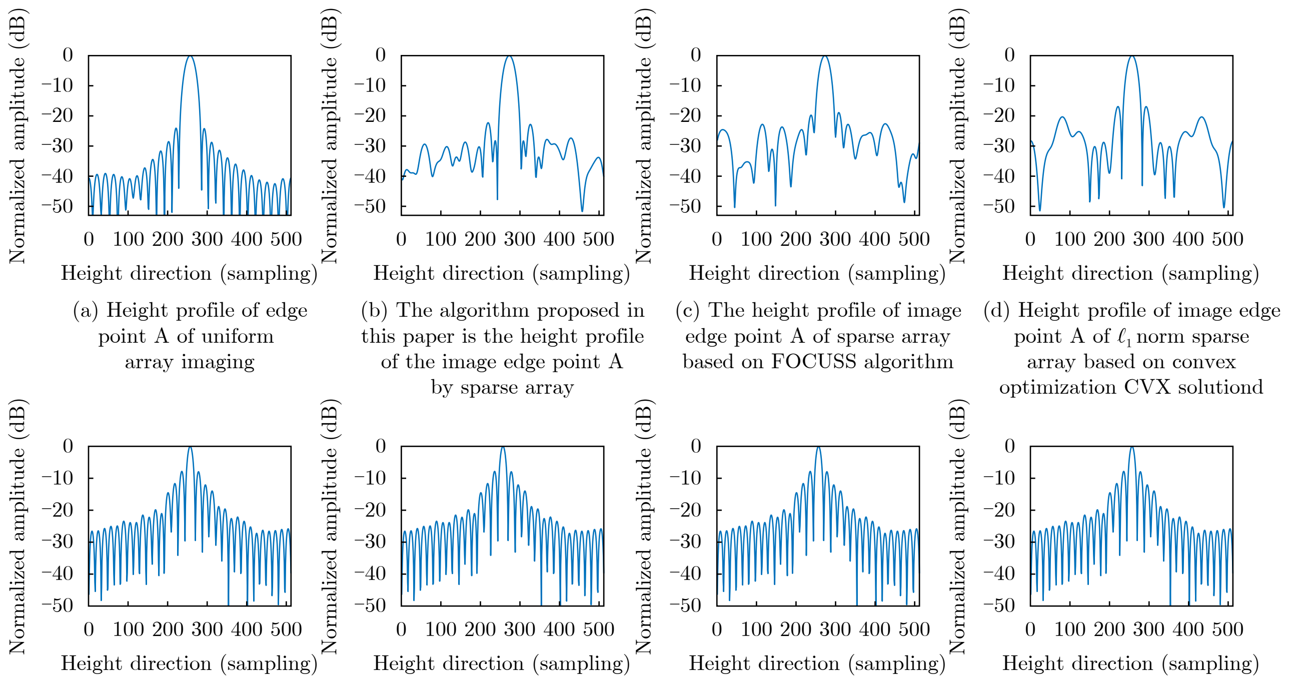

(a) Height profile of edge point A of uniform array imaging

(b) The algorithm proposed in this paper is the height profile of the image edge point A by sparse array

(c) The height profile of image edge point A of sparse array based on FOCUSS algorithm

(d) Height profile of image edge point A of ℓ_1 norm sparse array based on convex optimization CVX solutiond

(e) Azimuth profile of edge point A of uniform array imaging

(f) The algorithm proposed in this paper is the azimuth profile of the image edge point A by sparse array

(g) The azimuthprofile of image edge point A of sparse array based on FOCUSS algorithm

(h) Azimuth profile of image edge point A of ℓ_1 norm sparse array based on convex optimization CVX solution

Fig. 15 Profile of edge points of imaging results of different sparse array synthesis algorithms

Tab. 3 Quantitative analysis of profile of edge points of imaging results by different sparse array synthesis methods

Imaging results of edge points	Height to peak sidelobe ratio (dB)	Height resolution (3 dB width) (mm)	Azimuthal peak sidelobe ratio (dB)	Azimuth Resolution (3 dB width) (mm)
Uniform array imaging	–24.69	7.76	–8.01	4.2
The algorithm proposed in this article for sparse array imaging	–22.15	7.76	–8.01	4.2
Sparse array imaging based on FOCUS algorithm	–20.18	7.79	–8.01	4.2
ℓ_1 Norm sparse array imaging based on convex optimization CVX solution	–17.98	7.82	–8.01	4.2

6 Conclusion

This paper has proposed a reliable inference near-field sparse comprehensive array 3D millimeter-wave imaging algorithm to address the contradiction between system cost, imaging accuracy, and imaging speed faced by millimeter-wave active scanning imaging systems. The algorithm is used to design a near-field sparse array that meets the expected directional pattern, and combined with an improved 3D time-domain imaging algorithm for reconstruction to verify the achievement of high-precision imaging at low system cost and complexity. In the sparse Bayesian learning framework, the near-field sparse array synthesis problem is modeled as a BCS problem. Probability and statistical models are performed using a reference direction map and error variables, and the complex excitation weights are hierarchically modeled. The posterior probability density function of the analytical complex excitation weights is obtained through the VB-EM algorithm, thereby obtaining high-order statistical information. Furthermore, the optimal value and dynamic range of the complex excitation weights are obtained, achieving a dynamic indication of the complex excitation weights. By comparing the sparse array designed by this algorithm with existing sparse array synthesis techniques, the effectiveness and superiority of the proposed algorithm, in terms of sparsity and matching accuracy have been demonstrated. Compared with uniformly spaced arrays, the sparse array designed in this paper can reduce the number of elements by about 29%. Finally, based on the measured data of 1D circumferential electrical scanning and 2D planar full electrical scanning, an improved 3D time-domain imaging algorithm was used for 3D reconstruction, verifying the advantages of the proposed algorithm in ensuring imaging results while reducing system complexity.

Conflict of Interests The authors declare that there is no conflict of interests

References

[1] MA Yuxin, HAI Yu, LI Zhongyu, *et al*. 3D high-resolution imaging algorithm with sparse trajectory for millimeter-wave radar[J]. *Journal of Radars*, 2023, 12(5): 1000–1013. doi: 10.12000/JR23001.

[2] MA Zhaohui, WANG Jingyang, JING Handan, *et al*. Millimeter wave security imaging based on single-channel MIMO radar[J]. *Journal of Infrared and Millimeter Waves*, 2020, 39(6): 709–717. doi: 10.11972/j.issn.1001-9014.2020.06.008.

[3] LIU Ke, ZHU Zezheng, YU Jun, *et al*. Sparse array design methods based on hole analysis of the coprime array[J]. *Journal of Electronics & Information Technology*, 2022, 44(1): 372–379. doi: 10.11999/JEIT201024.

[4] KARIMKASHI S and KISHK A A. Focused microstrip array antenna using a Dolph-Chebyshev near-field design[J]. *IEEE Transactions on Antennas and Propagation*, 2009, 57(12): 3813–3820. doi: 10.1109/TAP.2009.2033435.

[5] ZHAO Lei, HUANG Kun, HAO Xin, *et al*. Non-uniform sparse array design in near field radar imaging[J]. *Journal of Terahertz Science and Electronic Information Technology*, 2017, 15(5): 707–710. doi: 10.11805/TKYDA201705.0707.

[6] ZHAO Dongdong, LIU Xuesong, CHEN Wenyuan, *et al*. Optimized design for sparse cross arrays in both near-field and far-field[J]. *IEEE Journal of Oceanic Engineering*, 2019, 44(3): 783–795. doi: 10.1109/JOE.2018.2837458.

[7] LEMAITRE-AUGER P, ABIELMONA S, and CALOZ C. Generation of Bessel beams by two-dimensional antenna arrays using sub-sampled distributions[J]. *IEEE Transactions on Antennas and Propagation*, 2013, 61(4): 1838–1849. doi: 10.1109/TAP.2012.2232263.

[8] LI Pengfa, QU Shiwei, YANG Shiwen, *et al*. Focused array antenna based on subarrays[J]. *IEEE Antennas and Wireless Propagation Letters*, 2017, 16: 888–891. doi: 10.1109/LAWP.2016.2613887.

[9] RUDOLPH D L and BAROTT W C. Reduction of near-field grating lobes in sparse linear phased arrays[C]. 2014 IEEE Antennas and Propagation Society International Symposium, Memphis, USA, 2014: 1155–1156. doi: 10.1109/APS.2014.6904904.

[10] OLIVERI G and MASSA A. Bayesian compressive sampling for pattern synthesis with maximally sparse non-uniform linear arrays[J]. *IEEE Transactions on Antennas and Propagation*, 2011, 59(2): 467–481. doi: 10.1109/TAP.2010.2096400.

[11] OLIVERI G, CARLIN M, and MASSA A. Complex-weight sparse linear array synthesis by Bayesian compressive sampling[J]. *IEEE Transactions on Antennas and Propagation*, 2012, 60(5): 2309–2326. doi: 10.1109/TAP.2012.2189742.

[12] YANG Lei, CHEN Yingjie, WANG Tengteng, *et al*. Three-dimensional reconstruction algorithm for passengers based on time-frequency coordination[J]. *Journal of Infrared and Millimeter Waves*, 2023, 42(3): 327–338. doi: 10.11972/j.issn.1001-9014.2023.03.006.

[13] CHEN Xiuqin, LI Yuehua, and KONG Lingxiong. Research on millimeter wave near field imaging and image enhancement algorithms[J]. *Journal of Microwaves*, 2023, 39(S1): 324–327.

[14] XIE Pengfei, ZHANG Lei, and WU Zhenhua. A three-dimensional imaging algorithm fusion with ω-K and BP algorithm for millimeter-wave cylindrical scanning [J]. *Journal of Radars*, 2018, 7(3): 387–394. doi: 10.12000/JR17112.

[15] LIN Zhenwei, CHEN Yaowu, LIU Xuesong, *et al*. Optimized design for sparse arrays in 3-D imaging sonar systems based on perturbed Bayesian compressive sensing[J]. *IEEE Sensors Journal*, 2020, 20(10): 5554–5565. doi: 10.1109/JSEN.2020.2971568.

[16] SONG Jiaqi and TAO Haihong. Near-field beam synthesis algorithm for sparse array antennas[J]. Journal of Xidian University: Natural Science, 2018, 45(6): 14–18. doi: 10.3969/j.issn.1001-2400.2018.06.003.

[17] HUANG Zixuan and CHENG Yujian. Near-field pattern synthesis for sparse focusing antenna arrays based on Bayesian compressive sensing and convex optimization[J]. *IEEE Transactions on Antennas and Propagation*, 2018, 66(10): 5249–5257. doi: 10.1109/TAP.2018.2860044.

[18] KIM S, DONG H J, YU J W, *et al*. Phased array calibration system with high accuracy and low complexity[J]. *Alexandria Engineering Journal*, 2023, 69: 759–770. doi: 10.1016/j.aej.2023.02.026.

[19] QI Zhengdong, LU Yangyi, KONG Yue, *et al*. Synthesis of sparse linear arrays based on multi-convex optimization[J]. *Radar & ECM*, 2019, 39(4): 21–24, 49. doi: 10.19341/j.cnki.issn.1009-0401.2019.04.006.

[20] BABACAN S D, MOLINA R, and KATSAGGELOS A K. Bayesian compressive sensing using Laplace priors[J]. *IEEE Transactions on Image Processing*, 2010, 19(1): 53–63. doi: 10.1109/TIP.2009.2032894.

[21] LIU Ying, ZHANG Zongyu, ZHOU Chengwei, *et al*. Robust variational Bayesian inference for direction-of-arrival estimation with sparse array[J]. *IEEE Transactions on Vehicular Technology*, 2022, 71(8): 8591–8602. doi: 10.1109/TVT.2022.3173418.

[22] ZHAO Xiaowen, YANG Qingshan, and ZHANG Yunhua. A hybrid method for the optimal synthesis of 3-D patterns of sparse concentric ring arrays[J]. *IEEE Transactions on Antennas and Propagation*, 2016, 64(2): 515–524. doi: 10.1109/TAP.2015.2504377.

[23] LI Haolin, CHEN Lulu, ZHANG Lei, *et al*. Study of autofocus method for SAR imagery created by fast factorized backprojection[J]. *Journal of Electronics & Information Technology*, 2014, 36(4): 938–945. doi: 10.3724/SP.J.1146.2013.00011.

[24] MA Chengzheng, YEO T S, LIU Zhoufeng, *et al*. Target imaging based on $\ell 1 \ell 0$ norms homotopy sparse signal recovery and distributed MIMO antennas[J]. *IEEE Transactions on Aerospace and Electronic Systems*, 2015, 51(4): 3399–3414. doi: 10.1109/TAES.2015.140939.

[25] YANG Peng, YAN Fei, ZHANG Shenghui, *et al*. Sparse array synthesis based on FOCUSS algorithm[J]. *Journal of University of Electronic Science and Technology of China*, 2014, 43(2): 203–206. doi: 10.3969/j.issn.1001-0548.2014.02.008.

[26] XING Mengdao, MA Penghui, LOU Yishan, *et al*. Review of fast back projection algorithmsin synthetic aperture radar[J]. *Journal of Radars*, 2024, 13(1): 1–22. doi: 10.12000/JR23183.

YANG Lei, PhD, is a professor, and doctoral supervisor, he mainly focuses on high-resolution SAR imaging and the theoretical application of machine learning.

HUO Xin, is a doctoral student, and mainly conducts research on millimeter-wave imaging and sparse array configuration design.

SHEN Ruiyang, is a master's student, and mainly conducts research on millimeter-wave imaging and sparse array configuration design.

SONG Hao, is a master's student, and mainly conducts research on millimeter-wave imaging and sparse array configuration design.

HU Zhongwei, PhD, is a lecturer, and master's supervisor, he mainly conducts research on high-resolution SAR imaging and optimization learning theory.

(Responsible Editor: YU Qing)